



HAL
open science

Role of crystallographic orientation on intragranular void growth in polycrystalline FCC materials

Paul Christodoulou, Sylvain Dancette, Ricardo Lebensohn, Eric Maire, Irene Beyerlein

► **To cite this version:**

Paul Christodoulou, Sylvain Dancette, Ricardo Lebensohn, Eric Maire, Irene Beyerlein. Role of crystallographic orientation on intragranular void growth in polycrystalline FCC materials. *International Journal of Plasticity*, 2021, 147, pp.103104. 10.1016/j.ijplas.2021.103104 . hal-03342622

HAL Id: hal-03342622

<https://hal.science/hal-03342622>

Submitted on 10 May 2022

HAL is a multi-disciplinary open access archive for the deposit and dissemination of scientific research documents, whether they are published or not. The documents may come from teaching and research institutions in France or abroad, or from public or private research centers.

L'archive ouverte pluridisciplinaire **HAL**, est destinée au dépôt et à la diffusion de documents scientifiques de niveau recherche, publiés ou non, émanant des établissements d'enseignement et de recherche français ou étrangers, des laboratoires publics ou privés.

Role of crystallographic orientation on intragranular void growth in polycrystalline FCC materials

Paul G. Christodoulou^{a,*}, Sylvain Dancette^b, Ricardo A. Lebensohn^c, Eric Maire^b, Irene J. Beyerlein^a

^a*Materials Department, University of California, Santa Barbara, Santa Barbara, 93117, CA, USA*

^b*MATEIS, CNRS UMR5510, INSA Lyon, Univ Lyon, 69100, Villeurbanne, France*

^c*Theoretical Division, Los Alamos National Laboratory, 87845, Los Alamos, NM, USA*

Abstract

In this work, we study the effect of crystallographic orientation and applied triaxiality on the growth of intragranular voids. Two 3D full-field micromechanics methods are used, the dilatational visco-plastic fast-Fourier transform (DVP-FFT) and the crystal plasticity Finite Elements (CP-FE), both of which incorporate a combination of crystalline plasticity and dilatational plasticity. We demonstrate with several select cases that predictions of void growth from both formulations agree qualitatively. With the more computationally efficient DVP-FFT, additional effects of polycrystalline microstructure and the influence of nearest neighborhood are investigated. Crystals bearing a single intracrystalline void are studied in three types of 3D microstructural environments: isolated single crystals, individual equal-sized grains within a regular polycrystal, and individual variable sized grains within a polycrystal with grains and voids randomly located. We show that loading type plays a significant role. In strain-rate controlled conditions, voids in the hardest [111]-crystals grow the fastest in time, whereas in stress-controlled conditions, voids in the softest [100]-crystal grow the fastest in time. The analysis reveals that on average void growth is slower for the same starting orientation in the polycrystal than in the single crystal. We

*Corresponding author

Email addresses: pchristodoulou@ucsb.edu (Paul G. Christodoulou), sylvain.dancette@insa-lyon.fr (Sylvain Dancette), lebenso@lanl.gov (Ricardo A. Lebensohn), eric.maire@insa-lyon.fr (Eric Maire), beyerlein@ucsb.edu (Irene J. Beyerlein)

find that at the highest triaxiality tested that the correlation between crystal orientation and void growth rate in the polycrystal strengthens, drawing closer to that seen in the isolated single crystals. These results and model can help guide the microstructural design of polycrystalline materials with high strength and damage-tolerance in high-rate deformation.

Keywords: A. Voids and Inclusions, B. Polycrystalline Material, B. Crystal Plasticity, B. Viscoplastic Material, C. Finite Elements,

1. Introduction

Over several decades, progress in the fundamental understanding of damage and failure of metallic materials has enabled the engineering of more reliable structural components. In most applications, metallic parts are polycrystalline aggregates made of anisotropic crystals of complicated shapes containing a variety of defects. This complexity determines microstructure-sensitive damage and failure behavior under thermo-mechanical processing. Recent advances in materials characterization techniques include *in situ* 3-D microscopic visualization of ductile damage due to porosity evolution, from nucleation to growth and coalescence of cavities. In polycrystalline materials, these techniques revealed a large diversity in void growth-rates likely due local crystalline environments [1, 2]. Despite these recent experimental observations, damage and failure models remain largely insensitive to local microstructural characteristics, due to a lack of consideration of the controlling processes at the scale of single crystals, whose elastic and plastic properties vary from grain to grain depending on orientation and, in some cases, are strongly anisotropic. Dealing with and quantifying these microstructural effects on ductile damage from a micromechanical perspective requires combining single crystal/polycrystal plasticity and dilatational plasticity models, which is the main focus of this work. When the metal contains inclusions, which is the case for most industrial alloys, damage nucleation is connected to these inclusions (e.g. Goods and Brown [3]) and these inclusions are not always located at grain boundaries, especially when grains are large. As a consequence, it is important to study intragranular growth of cavities.

Crystal plasticity (CP) models, which approximates plastic deformation accommodated by dislocation slip in single crystals, have been combined with the finite element (FE) method (e.g. Roters et al. [4]) to account for spatial variations of mechanical properties of fully-dense polycrystalline materials.

The implementation of CP constitutive behavior in FFT-based formulations, conceived as an efficient alternative to CP-FE (e.g. Lebensohn [5], Lebensohn et al. [6] in the rigid-viscoplastic (VP-FFT) regime, Lebensohn et al. [7] and Eisenlohr et al. [8] in the small-strain and large-strain elasto-viscoplastic (EVP-FFT) regimes), has enabled fine-scale microstructural information in polycrystalline materials to be accounted for with an unprecedented level of detail.

Analytical dilatational plasticity models, on the other hand, describe the growth of a cavity in a plastically deforming homogeneous matrix. These models are largely based on the analysis of the mechanical response of a hollow sphere with isotropic rigid-perfectly plastic behavior and were pioneered by Rice and Tracey [9] and Gurson [10], and have been generalized to consider different geometries and material behavior [11–18]. Other analytical homogenization methods were extended to the problem of dilatational plasticity [19, 20]. Concurrently, FE-based cell calculations have been used extensively, either in purely numerical studies, or for validation and calibration of analytical dilatational plasticity models, including the study of void growth in single crystals [21–25]. A number of similar studies conduct simulations on single crystals and a singular void at a grain boundary or triple junction [26, 27]. These integrated dilatational/single crystal plasticity analyses and numerical calculations showed that the directionality of the plastic response of the single crystal strongly affect void growth. However, the ideal configurations considered by the aforementioned analytical and numerical dilatational plasticity models are unable to capture the complex way in which the microstructure of polycrystalline materials affects damage evolution associated with void growth. For such more realistic configurations, analytical expressions are not available and numerical models are very limited. Analytical model extensions may be adopted to capture some effects related polycrystalline character of the matrix, e.g. texture-induced plastic anisotropy, by first homogenizing the polycrystalline matrix’s properties and then applying anisotropic extensions of limit-analysis models [15, 16, 18]. Liu et al. [28] conducted a series of CP-FE simulations on a single void in a heterogeneous FCC polycrystal with random orientations. They found that macroscopic triaxiality played an important role in the growth of voids, and that at lower triaxialities, the effect of the orientation of the crystals around the void had a greater effect on the void growth, particularly the dispersion of said growth between individual simulations. Ultimately, they proposed a statistical micro void growth model to capture the dispersion of the results

from the study. There is relatively little studied on orientation effects within polycrystals. One exception is this study Liu et al., although the study used only CPFEM, and only includes one void in the central grain with a cuboid arrangement of grains. In addition, less orientations are simulated than in the current study.

Only a handful of numerical simulations have dealt with configurations involving multiple interacting voids. In the context of FE, Fritzen et al. [29] investigated the effective material response of metals with multiple spherical voids for different volume fractions with varying loading types. It was found that the Gurson-Tvergaard-Needleman [30] analytical model only required one additional parameter to efficiently predict the macroscopic stress for all examined porosities. Ghosh et al. [31] performed FE calculations on a metal with hard inclusions and individual, albeit isotropic, domains representing grains. The source of the heterogeneity was the voids that eventually formed near the inclusions.

In the context of FFT-based models, Bilger et al. [32] performed calculations on isotropic, perfectly-plastic materials with voids in various configurations to determine the effect of the void distribution on yielding. These simulations showed that the clustering of voids reduced the yield strength of the material, which motivated Bilger et al.'s [33] proposal of analytical expressions to predict the yield stress of a material using a clustering parameter. However, they found that at high triaxialities, the yield strength was difficult to predict in microstructures with highly clustered voids. None of these models, neither in FEA nor FFT-based simulations, used crystal plasticity, and as such lacked the ability to account for crystal orientation.

Lebensohn et al. [34] and Vincent et al. [35] used FFT-based methods with explicit representation of voids in polycrystalline and isotropic matrices, respectively, but their analysis was limited to fixed configurations, i.e. studying the dilatational plastic response under different applied stress conditions, but without porosity evolution. Lebensohn et al. [36] extended the VP-FFT formulation to account for dilatational effects (resulting in dilatational viscoplastic (DVP-FFT) formulation) associated with the presence of intergranular voids in a polycrystalline matrix. This DVP-FFT model included specific algorithms inspired by the particle-in-cell (PIC) method (e.g. Sulsky and Schreyer [37], FFT-based implementation of Lahellec et al. [38]) to take porosity evolution into account. DVP-FFT calculations allowed, for the first time, consideration of microstructural effects on porosity growth-driven ductile damage, with crystals and voids represented explicitly. In particu-

lar, DVP-FFT calculations were performed on two materials with identical initial porosity distribution: one representing an FCC polycrystal with uniform texture and intergranular cavities, and the other representing a porous material with homogenous isotropic matrix. Comparative calculations were performed on these two materials to study the effect of the matrix's polycrystallinity on porosity evolution. Although intragranular growth of cavities in single crystals is a widely studied topic, our findings are not completely in line with some previous results and, to the authors' knowledge, no CPFE vs. FFT comparisons have been conducted within this field. In addition, a very limited number address void growth in polycrystals, and none attempting to decorrelate the effect of crystallographic orientation and grain neighborhood as we have done here.

In this work, we study the effect of crystallographic orientation and applied triaxiality on the growth of intragranular spherical voids. Note that we focus on the void growth stage of ductile damage, assuming pre-existing voids that have already nucleated in the interior of crystals/grains, and not considering the late stage of void coalescence. We employ the DVP-FFT and CPFE formulations, which both incorporate a combination of crystalline plasticity and dilatational plasticity and permit explicit representation of intracrystalline voids. Such voids would occur, for example, by decohesion or fracture of second-phase particles in the grain interiors of engineering materials. For several single crystal orientations and triaxialities, we demonstrate that predictions of void growth from both formulations agree reasonably well. Based on this cross-validation, we proceed to employ the more computationally efficient DVP-FFT to investigate intragranular void growth in polycrystalline microstructures, wherein every crystal contains a single intragranular void. We show that whether the loading type is full-stress controlled or longitudinal strain-rate/stress-triaxiality controlled plays a significant role of the orientation vs. growth rate relationship. In strain-rate controlled conditions, voids in the hardest [111]-crystals grow the fastest in time, whereas in stress-controlled conditions, voids in the softest [100]-crystal grow the fastest in time. The implications of these results are discussed, particularly focusing on the interplay between orientation, triaxiality, and loading types.

The plan of the paper is as follows: In section 2 we present relevant details on the basics and modifications of the DVP-FFT and CP-FE to account for dilatational effects in single crystals and polycrystals with intragranular cavities, as well as the simulations conducted to probe the effect of lattice orientation on intragranular void growth. Section 3 presents a comparison

of void growth in single crystals under axisymmetric tension, with different crystal orientations aligned with the major tensile axis and different stress triaxialities, predicted with DVP-FFT and CP-FE, followed by a comprehensive study of orientation effects on intragranular void growth using DVP-FFT in both single crystals and polycrystals. The implications of these results are discussed in the same section, particularly focusing on the interplay between orientation, triaxiality, and loading types. Finally, key takeaways of this study and outstanding questions are addressed in Section 4.

2. Method and Simulation Procedures

2.1. Single crystal viscoplastic behavior

In the current configuration, the viscoplastic behavior of a single crystal material point is described by means of the following non-linear, incompressible, rate-sensitive equation relating the Cauchy stress $\boldsymbol{\sigma}$ and the Eulerian plastic strain rate $\dot{\boldsymbol{\epsilon}}$ at point \mathbf{x} :

$$\dot{\boldsymbol{\epsilon}}(\mathbf{x}) = \sum_{k=1}^K \mathbf{m}^k(\mathbf{x}) \dot{\gamma}^k(\mathbf{x}) = \dot{\gamma}_0 \sum_{k=1}^K \mathbf{m}^k(\mathbf{x}) \left(\frac{|\mathbf{m}^k(\mathbf{x}) : \boldsymbol{\sigma}(\mathbf{x})|}{\tau^k(\mathbf{x})} \right)^n \text{sgn}(\mathbf{m}^k(\mathbf{x}) : \boldsymbol{\sigma}(\mathbf{x})) \quad (1)$$

with $\dot{\gamma}^k(\mathbf{x})$, $\tau^k(\mathbf{x})$, and $\mathbf{m}^k(\mathbf{x}) = \frac{1}{2} (\mathbf{n}^k(\mathbf{x}) \otimes \mathbf{b}^k(\mathbf{x}) + \mathbf{b}^k(\mathbf{x}) \otimes \mathbf{n}^k(\mathbf{x}))$ being, respectively, the shear rate, the critical resolved shear stress, and the symmetric part of the Schmid tensor, associated with each slip system k of the K systems available, where \mathbf{n}^k and \mathbf{b}^k are the normal and Burgers vector direction of such slip system, $\dot{\gamma}_0$ is a reference rate, and n is the stress exponent.

If the shear rates $\dot{\gamma}^k(\mathbf{x})$ can be considered constant in a time increment Δt such that $\Delta \gamma^k(\mathbf{x}) = \dot{\gamma}^k(\mathbf{x}) \Delta t$, the critical stresses of the deformation systems can be explicitly updated due to strain hardening. Here we use an extended Voce law (Tomé et al. [39]), such that the evolution of the critical stress with accumulated shear strain in each grain is given by:

$$\tau^k(\mathbf{x}) = \tau_0^k + (\tau_1^k + \theta_1^k \Gamma(\mathbf{x})) (1 - \exp(-\Gamma(\mathbf{x}) |\theta_0^k / \tau_1^k|)) \quad (2)$$

where $\Gamma(\mathbf{x}) = \sum_{k=1}^K \gamma^k(\mathbf{x})$ is the total accumulated shear in the grain, and τ_0^k , τ_1^k , θ_0^k , and θ_1^k are the initial threshold stress, the initial hardening rate, the asymptotic hardening rate, and the back-extrapolated threshold stress, respectively.

2.2. DVP-FFT formulation

FFT-based formulations are spectral numerical methods to compute the local and effective response of heterogeneous materials, solving the governing equations inside a periodic unit cell that give an equilibrated stress field constitutively related to a compatible strain field. The heterogeneity of the unit cell may come from the presence of different isotropic phases, as in the case of composites, different grain orientations, as in the case of polycrystals, or a combination of both, i.e. multiphase polycrystalline materials. Porous polycrystals are a special case of the latter, in which one of the phases is the void phase, which cannot sustain stress. The starting point to combine crystal plasticity and dilatational effects has been the rigid-viscoplastic VP-FFT formulation (Lebensohn et al. [5, 6]) for fully-dense polycrystalline aggregates with single crystals obeying the constitutive equation given in equation 1. With the addition of voids, the latter incompressible formulation was extended (Lebensohn et al. [34]), resulting in the DVP-FFT model to compute the instantaneous dilatational viscoplastic behavior of porous polycrystals. The addition of algorithms to account for void growth based on the use a Lagrangian grid of material points on top of the Eulerian computational regular grid where FFTs are performed (Lahellec et al. [38]), allowed extending DVP-FFT to predict porosity evolution in voided polycrystals, as well as porous materials with homogenous rigid-viscoplastic isotropic matrix (Lebensohn et al. [36]). The extension of the latter to consider porosity evolution in single crystals is straightforward, adopting the constitutive equation (equation 1) for materials points belonging to the single crystal matrix.

We generate the material points by first considering a regularly-spaced set of $2N_1 \times 2N_2 \times 2N_3$ voxels that discretize the unit cell and have single-crystal rigid-viscoplastic properties (equation 1). These properties can be homogeneous throughout the entire unit cell (single crystal case) or periodically heterogeneous (polycrystal case). Next, we seed the void phase using certain criteria, as described in section 2.4) by removing the voxels occupied by the voids from the set of materials points. The points remaining in the material phase represent a set of material points denoted as $\{\mathbf{x}^M\}$. Next, every other point of the regular grid along the three directions is identified as Fourier points, resulting in a $N_1 \times N_2 \times N_3$ computational grid, to be denoted $\{\mathbf{x}\}$. This Fourier grid in Cartesian space has a corresponding grid of the same size in Fourier space $\{\mathbf{k}\}$. When a strain rate $\dot{\mathbf{E}}$, or a stress Σ , or a combination of both is applied to the unit cell, the local strain rate field is a function of the local velocity field, and can be split into its average and a

fluctuation term:

$$\dot{\epsilon}_{ij}(\mathbf{v}(\mathbf{x})) = \dot{E}_{ij} + \tilde{\epsilon}_{ij}(\tilde{\mathbf{v}}(\mathbf{x})) \quad (3)$$

where:

$$v_i(\mathbf{x}) = \dot{E}_{ij}x_j + \tilde{v}_i(\mathbf{x}) = V_i(\mathbf{x}) + \tilde{v}_i(\mathbf{x}) \quad (4)$$

The local constitutive relation between the strain rate and the stress for Fourier points with single crystal properties is given by equation 1. The strain rate at these points has no dilatational component. As for the Fourier points belonging to voids, the stress vanishes. In FFT-based formulations, a fourth-order tensor \mathbf{L}^o is the stiffness of a linear reference medium, and the polarization field is given as:

$$\phi_{ij}(\mathbf{x}) = \tilde{\sigma}_{ij}(\mathbf{x}) - L_{ijkl}^o \tilde{\epsilon}_{kl}(\mathbf{x}) \quad (5)$$

such that the stress fluctuation is written as:

$$\tilde{\sigma}_{ij}(\mathbf{x}) = L_{ijkl}^o \tilde{\epsilon}_{kl}(\mathbf{x}) + \phi_{ij}(\mathbf{x}) \quad (6)$$

Combining equation 6 with the equilibrium condition: $\sigma_{ij,j}(\mathbf{x}) = \mathbf{0}$ and $\tilde{\epsilon}_{kl}(\mathbf{x}) = \text{sym}(\tilde{v}_{k,l}(\mathbf{x}))$ gives:

$$L_{ijkl}^o \tilde{v}_{k,l,j}(\mathbf{x}) + \phi_{ij,j}(\mathbf{x}) = \mathbf{0} \quad (7)$$

The differential equation whose solution is the Green's function G_{km} associated with the velocity field is then given by:

$$L_{ijkl}^o G_{km,lj}(\mathbf{x} - \mathbf{x}') + \delta_{im} \delta(\mathbf{x} - \mathbf{x}') = \mathbf{0} \quad (8)$$

where δ_{im} and $\delta(\mathbf{x})$ are the Kronecker and Dirac delta functions, respectively. The convolution integral that gives the velocity field is:

$$\tilde{v}_i(\mathbf{x}) = \int_{R^3} G_{ik,l}(\mathbf{x} - \mathbf{x}') \phi_{kl}(\mathbf{x}') d\mathbf{x}' \quad (9)$$

Applying the convolution theorem, the velocity and velocity gradient fields in Fourier space are given by:

$$\hat{\tilde{v}}_i(\mathbf{k}) = (-ik_l) \hat{G}_{ik}(\mathbf{k}) \hat{\phi}_{kl}(\mathbf{k}) \quad (10)$$

$$\hat{\tilde{v}}_{i,j}(\mathbf{k}) = \hat{\Gamma}_{ijkl}(\mathbf{k}) \hat{\phi}_{kl}(\mathbf{k}) \quad (11)$$

where the symbol “ $\hat{}$ ” indicates Fourier transform, and $\Gamma_{ijkl} = G_{ik,jl}$, which, using the definition of the Green’s function, can be calculated in Fourier space as (see Lebensohn [5] for details on derivation):

$$\hat{G}_{ik}(\mathbf{k}) = A_{ik}^{-1}(\mathbf{k}), \text{ where: } A_{ik}(\mathbf{k}) = k_j k_l L_{ijkl}^o, \text{ and: } \hat{\Gamma}_{ijkl}(\mathbf{k}) = -k_j k_l \hat{G}_{ik}(\mathbf{k}) \quad (12)$$

Note that with $\hat{\Gamma}_{ijkl}(\mathbf{k})$ from equation 12, and the current value of the polarization field in Fourier space, the symmetric part of equation 11 gives the new guess of the strain-rate fluctuation field, which can then be antitransformed to obtain the associated new stress fluctuation field by evaluating the local constitutive equation. These updated guesses for the strain-rate and stress fluctuation fields can in turn be used in equation 5 to update the polarization field, and so on and so forth.

From these equations, an iterative procedure based on the augmented Lagrangian algorithm (Michel et al. [40]) is adapted and adopted for the case of porous single crystals (this work), and polycrystals (see Lebensohn et al. [34]). Upon convergence, the stress and strain-rate fluctuation fields are added to the macroscopic stress and strain-rate tensors, which satisfy the applied boundary conditions (see Lebensohn et al. [34] for details).

Also upon convergence, the critical stresses of the Fourier points with single crystal properties can be explicitly updated according to the strain hardening law using equation 2. The lattice rotation rate field can be also obtained (see Lebensohn et al. [36] for details). This field, if assumed constant over the time increment Δt used to march in time, can be integrated and used to update the crystallographic orientations associated with the points in the Fourier grid $\{\mathbf{x}\}$ with single crystal properties. Interpolation between $\{\mathbf{x}\}$ and the set of material points $\{\mathbf{x}^M\}$ (see Lebensohn et al. [36]) allow updating the critical stresses and crystallographic orientations of the latter, resulting in strain-hardening and texture evolution.

Equation 4 and the anti-transformation of equation 10 give the time integration and interpolation of the velocity field mapped onto the Fourier grid. Together, they provide the local displacements of the material points, which scale with Δt . Under positive triaxialities, porosity will increase and the aforementioned displacements will be such that the material points will move away from neighboring voids. This will result in a local incompressible strain, dependent on the local single crystal plastic anisotropy and microstructure. The corresponding void growth accommodates the volume change imposed to the unit cell, which is given by $\dot{E}_{kk} \Delta t$. The new positions of the material

points can be used as input of an algorithm (see Lebensohn et al. [36]) to reassign void properties to certain Fourier points (i.e. those whose distance to the nearest material point becomes higher than a threshold), which previously had material properties. This reassignment determines local void growth, and contributes to the overall porosity increase. As part of this algorithm, the time increment Δt can be controlled, such that the change in macroscopic porosity f given by $\Delta f = (1-f) \dot{E}_{kk} \Delta t$ (Tvergaard’s formula [41]) coincides with the average of local porosity changes.

In this work, DVP-FFT simulations for two types of imposed loads are presented. The first one, used only in section 3.2 to precisely understand the influence of different loading types, is fully-imposed stress Σ (therefore also imposing stress triaxiality), which corresponds to the algorithm previously described. The other type of loading type, used throughout the paper is the one used by Ling et al. [24], in which the stress triaxiality is imposed (i.e. the ratio between stress components, but not the magnitude of stress itself) along with the longitudinal component of the strain-rate. The latter loading type requires a correction to the stress tensor applied to the unit cell, based on the consideration of the homogeneity of degree n of the strain-rate response to a given applied stress, explained as follows. For a porous material with single crystal or polycrystal matrix, whose local material behavior is given by equation 1, if $\dot{E}^{(1)}$ is a scalar measure (e.g. longitudinal component) of the strain rate response to a stress tensor $\Sigma^{(1)}$ applied to the unit cell, then the imposed stress can be corrected according to $\Sigma^{(2)} = \left(\dot{E}^{(2)} / \dot{E}^{(1)} \right)^{1/n} \Sigma^{(1)}$ to obtain a strain rate response with $\dot{E}^{(2)}$ longitudinal component.

2.3. FEM formulation

The finite element model of the voided single crystal problem consists of a FE mesh of a periodic unit cell with a void in the center (figure 1) and a single crystal plasticity subroutine [42, 43] to compute the constitutive response at the level of the FE integration points, within the framework of an Abaqus-Implicit solver.

The control of both strain rate and stress triaxiality is achieved in the FE model by the use of dummy nodes connected by linear springs outside of the unit cell for the control of boundary conditions (Figure 1.a), as inspired from the work of Lecarme et al. [44]. The FE mesh of the cuboidal single crystal unit cell is periodic, in the sense that the node coordinates on each opposite outer surfaces are related by a translation. Periodic boundary conditions are

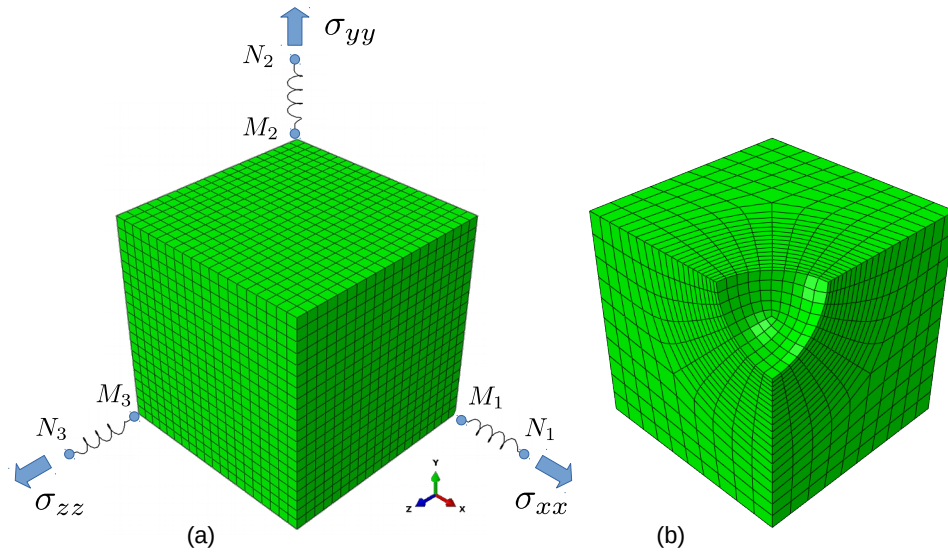


Figure 1: (a) Finite element setup for strain-rate and stress-triaxiality controlled loading of the porous unit cells containing a central cavity and composed of Abaqus C3D8 brick elements. Axial strain rate is imposed by displacement of node N_3 , while the stress triaxiality and the axisymmetric stress condition are controlled by the displacements of node N_1 and N_2 in equations 18 and 19 (Abaqus nodal MPC). (b) One eighth of the unit cell highlighting the central cavity ($f=0.01$).

applied by coupling the displacement degrees of freedom (DOF) of node pairs that face each other through the displacement of the master nodes M_1 , M_2 and M_3 in Figure 1.

Assuming an axisymmetric stress state with z as the primary loading direction and using the definitions of the mean (hydrostatic) stress σ_H and the Von Mises equivalent stress σ_{eq} , the stress triaxiality $T = \frac{\sigma_H}{\sigma_{eq}}$ reduces to:

$$T = \frac{2\sigma_{xx} + \sigma_{zz}}{3(\sigma_{zz} - \sigma_{xx})} \quad (13)$$

which can be re-arranged to express σ_{xx} as a function of the primary stress σ_{zz} :

$$\sigma_{xx} = \sigma_{zz} \frac{3T - 1}{3T + 2} \quad (14)$$

The forces exerted on the faces of the unit cell by the springs (with identical stiffness K) is written:

$$F_x = K(u_x^{N_1} - u_x^{M_1}), \quad F_y = K(u_y^{N_2} - u_y^{M_2}), \quad F_z = K(u_z^{N_3} - u_z^{M_3}) \quad (15)$$

The instantaneous area of the faces of the unit cells can be written as a function of the initial edge length L_0 of the unit cell and the displacement of the master nodes M_1 , M_2 , and M_3 shown in Figure 1:

$$\begin{aligned} S_x &= (L_0 + u_y^{M_2})(L_0 + u_z^{M_3}) \\ S_y &= (L_0 + u_x^{M_1})(L_0 + u_z^{M_3}) \\ S_z &= (L_0 + u_y^{M_2})(L_0 + u_x^{M_1}) \end{aligned} \quad (16)$$

from which the instantaneous (true) stress components can be written as:

$$\sigma_{xx} = \frac{F_x}{S_x}, \quad \sigma_{yy} = \frac{F_y}{S_y}, \quad \sigma_{zz} = \frac{F_z}{S_z} \quad (17)$$

To satisfy the stress triaxiality constraint of equation 14, equations 15, 16, and 17 can be combined and inserted into equation 14 to yield the following expression of $u_x^{N_1}$:

$$u_x^{N_1} = u_x^{M_1} + B \frac{(L_0 + u_z^{M_3})(u_z^{N_3} - u_z^{M_3})}{L_0 + u_x^{M_1}} \quad (18)$$

where B stands for $\frac{3T-1}{3T+2}$.

Moreover, when the axisymmetric stress state condition, $\sigma_{xx}=\sigma_{yy}$, is satisfied, the following expression of $u_y^{N_2}$ results:

$$u_y^{N_2} = u_y^{M_2} + \frac{(L_0 + u_x^{M_1})(u_x^{N_1} - u_x^{M_1})}{L_0 + u_y^{M_2}} \quad (19)$$

While $u_z^{N_3}$ is prescribed to achieve the desired axial strain-rate of the unit cell, equations 18 and 19 are solved iteratively using an Abaqus Multi-Point Constraint (nodal MPC), coded as a Fortran user subroutine.

The crystal plasticity constitutive behavior is computed with a user subroutine, which is summarized below (see [42, 43] for more details). The stress developed in the crystals at each integration point is obtained based on the multiplicative decomposition of the deformation gradient tensor $\mathbf{F}=\mathbf{R}^*\mathbf{U}^{el}\mathbf{F}^p$, where \mathbf{R}^* is the lattice rotation, $\mathbf{U}^{el}=1+\boldsymbol{\epsilon}$ is an infinitesimal elastic stretch, and \mathbf{F}^p is the result of dislocation slip (plastic deformation). The velocity gradient tensor \mathbf{L} is:

$$\mathbf{L} = \dot{\mathbf{F}}\mathbf{F}^{-1} \simeq \dot{\mathbf{R}}^* \mathbf{R}^{*T} + \mathbf{R}^* (\dot{\boldsymbol{\epsilon}} + \mathbf{L}^p) \mathbf{R}^{*T} \quad (20)$$

where

$$\mathbf{L}^p = \dot{\mathbf{F}}^p \mathbf{F}^{p-1} = \sum_k (\mathbf{b}^k \otimes \mathbf{n}^k) \dot{\gamma}^k \quad (21)$$

The slip rate $\dot{\gamma}^k$ on slip system k and the hardening rule for the critical resolved shear stress τ^k are calculated as detailed in section 2.1. The elastic part of the strain rate $\dot{\boldsymbol{\epsilon}}$ is related to the elastic stiffness tensor and the time-derivative of the second Piola-Kirchhof stress computed in the intermediate configuration. Lattice rotation \mathbf{R}^* is calculated by the time-integration of the skew-symmetric part of the velocity gradient \mathbf{L} (equation 20).

In summary, the FFT-based and FE crystal plasticity formulations at the material points are similar, but differ by the consideration of a (relatively small, compared with the viscoplastic part) elastic contribution to the total deformation in the CP-FE approach, which is neglected in DVP-FFT computations. Moreover, the adopted CP-FE is based on large-strain kinematics (equations 20 and 21), while DVP-FFT microstructure (including porosity evolution) is based on the combined use of a Lagrangian set of material points and an Eulerian computational grid, as described in the previous sub-section.

2.4. Simulations designed to probe orientation dependence

In this section, we describe the different simulations conducted to determine the effect of crystal orientation on void growth employing the DVP-FFT and CP-FE formulations. Three groups of microstructures were employed to probe the orientation dependence of intracrystalline void growth under axisymmetric tension: one group of single crystal simulations, and two groups of polycrystalline simulations, shown in Figure 2. All simulations employed a set of 72 predetermined orientations of the crystal axes with respect to the tensile axis: 45 orientations originally introduced by Lebensohn et al. [45], and 27 additional orientations to cover the intermediate regions of orientation space between the [100], [101], and [111] orientations, shown in Figure 2b. These 27 orientations are not as evenly spaced as the original 45 orientations, but they cover the missing regions without duplication. These selected orientations are presented in an inverse pole figure/stereographic triangle relative to the z -direction, i.e. the axis of the largest principal stress in our simulations.

The first set of simulations conducted using DVP-FFT and CP-FE consider single crystalline unit cells. CP-FE is used here to compare to DVP-FFT and verify its results in simple cases. For the majority of simulations that follow, the DVP-FFT is employed because of its computational efficiency and that it is a much easier way to discretize and treat complex structures. In the DVP-FFT simulations, 72 individual voided single crystals were created and the corresponding unit cells were discretized with $128 \times 128 \times 128$ material points (minus those in the void region), corresponding to a Fourier grid size of 64 in each direction, with the void at the center of the simulation, occupying 1% of the volume of the initial crystal. The selected percentage permitted a sufficient amount of observable voxel points and grid refinement (i.e., we had spherical voids) without initiating significant void-to-void interaction. The difference between the grid employed in this work and that of a finer one are approximately 3% in axial stress and less than 1% in void fraction and void fraction growth rate. Each single crystalline unit cell had an orientation corresponding to one of the 72 orientations described above. Of the 72 unit cells, four single crystal orientations were compared against corresponding CP-FE simulations: [100], [101], [111], and [210] orientations. The CP-FE single crystal unit cells were composed of 16000 Abaqus C3D8 brick elements (eight nodes, eight integration points). Convergence of the CP-FE results was checked with respect to the number and type of finite elements used to mesh the unit cell. The chosen orientations also allowed

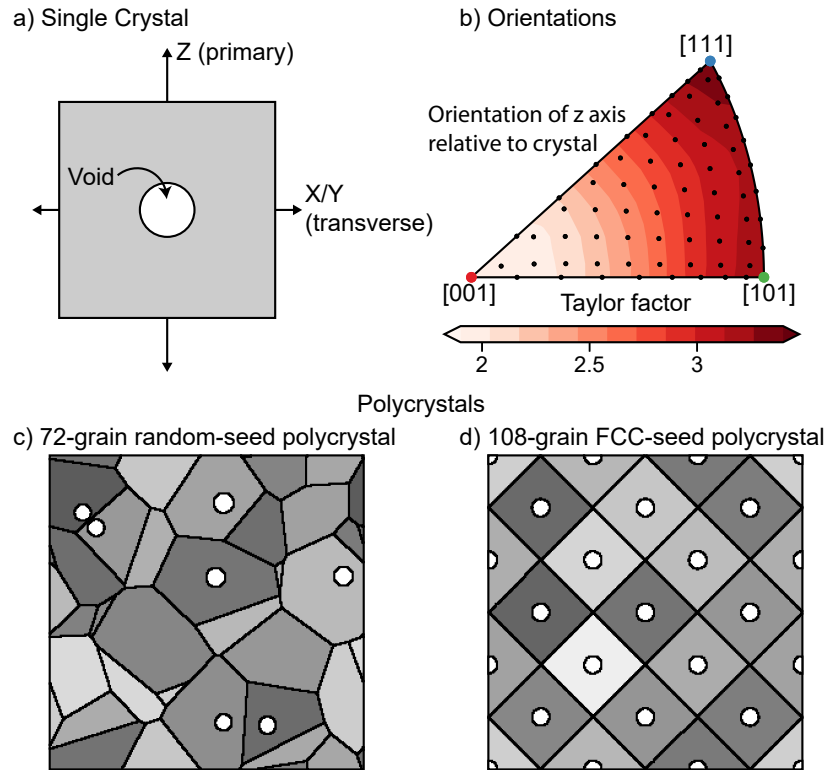


Figure 2: Figures of the three 3-dimensional microstructure sets used in the simulations: (a) a periodic single crystal with a void in the interior, with a primary stress in the Z direction; (b) the 72 key crystal orientations used in the simulations (as dots), and are colored with the Taylor Factor of the fully dense material calculated for a $n=5$; and (c) and (d) are the two polycrystalline microstructures. Sub-figure (c) is a 2-D slice through the random 72-grain voronoi tessellation with voids at the seed of each of the Voronoi cells. Sub-figure (d) shows a 2D slice through the plane of the 108-void system, in which the voids are placed in an FCC-like array and the grains form the Wigner-Seitz cells around each void. The center of the grain and the center of the void coincide in this regular grid, and the grains form dodecahedrons, consistent with a coordination number of 12. In each case, the boundary conditions are the same as in (a), with the primary axis is in the Z direction.

qualitative comparison with previously reported CP-FE simulations by Ling et al. [24].

Besides voided single crystals, we studied polycrystalline microstructures with intragranular voids as well, in order to access nearest grain neighborhood effects. Two sets of polycrystalline microstructures were simulated using DVP-FFT. Both types were composed of $256 \times 256 \times 256$ material points before removing those from the voids, corresponding to $128 \times 128 \times 128$ Fourier points. The first microstructure was a 72-grain unit cell, with the grains randomly-generated by periodic Voronoi tessellation. Voids were located at the seed points of the Voronoi structure, and occupied 1% of that grain's volume, i.e. larger grains contained larger voids. 72 random orientations were assigned to the grains. The same 72-grain partition was used in different realizations to maintain the same morphology, while the orientations assigned to each grain were randomly reassigned, for a total of 30 realizations.

The second type of polycrystalline microstructures, and the third microstructure group, was created by placing the center of the voids in an FCC-type super-lattice (i.e. regular arrangement of grains, not of atoms), and forming the grains around them, using their Wigner-Seitz cells. This placement ensured that all voids were at the center of the grains, and that all voids were identical in shape and size, reducing the variables to the individual grains orientation and neighborhood. However, because the microstructures needed to have four (for one FCC unit cell) voids, and power-of-three numbers of FCC super-cells are convenient, 108 voided grains were created (4×36). The 72 orientations were randomly assigned to 72 of the 108 grains, and the remaining 36 grains were randomly assigned 36 random orientations. As before, these 108 orientations were randomly assigned in 30 separate realizations.

All simulations were stress-triaxiality controlled and of these, most were additionally strain-rate controlled, while a small group of six simulations were instead stress-controlled (reasons to be discussed shortly). The applied strain rate in strain-rate controlled simulations was $\dot{\epsilon}_{eq}^p = 1.0 \text{ s}^{-1}$ in the DVP-FFT, and $\dot{\epsilon}_{33}^p = 1.0 \text{ s}^{-1}$ in the FEA. Each microstructure was simulated using DVP-FFT at four stress triaxialities: $T_X = 0.6, 1, 2,$ and 3 , with the primary axis along the z -direction, and axisymmetric stresses in the x and y -directions. FEM simulations will be presented at two of those four triaxialities: $T_X = 0.6$ and 3 . Not all of the results will be presented, given that the intermediate triaxialities were found to represent intermediate states between the lowest and highest triaxialities.

A set of single-crystal simulations at the highest and lowest stress triaxiality but with fully-prescribed equivalent stress of $\sigma_{eq}=2.5\tau_0$ were additionally conducted with DVP-FFT. Only the [100], [101], and [111] single crystal orientations were simulated. These simulations are discussed in section 3.2.

The crystals were able to plastically deform activating the 12 $\langle 110 \rangle \{111\}$ slip systems associated with FCC slip. The reference slip rate and stress exponent in equation 1, are $\dot{\gamma}_0=1.0$ and $n=5$, respectively. The Voce hardening parameters from the equation 2 were $\tau_0=1.0$ MPa, $\tau_1=3.0$ MPa, $\theta_0=8.0$ MPa, and $\theta_1=0.0$ MPa. Additionally, in the FEM calculations, isotropic elastic coefficients were assumed: $C_{11} = 1346$ MPa, $C_{12} = 577$ MPa and $C_{44} = 385$ MPa, resulting in a Young's modulus more than 1000 times larger than τ_0 .

3. Results & Discussion

3.1. Voids in single crystals, comparisons between CP-FE and DVP-FFT

To ascertain that the CP-FE and DVP-FFT models show the same void growth trends, single crystal simulations were compared for the highest and lowest triaxialities ($T_X=0.6$ and $T_X=3$). Figure 3 shows the normalized void volume, V/V_0 ; remote stress, σ_{33}/τ_0 ; and transverse plastic strain, ε_T^p , as a function of plastic strain in the axial direction, ε_{33}^p at the lowest triaxiality. The stresses and transverse strains are within 10% of each other at strains above 0.2 for the lower triaxiality simulations. The volume fraction of the voids, except for voids in the [101]-oriented crystals, differ by less than 10% at all strains. The voids in the [101]-oriented crystals differ by less than 10% up to strains of 0.5, and then increase to 25% by 100% axial strain.

The DVP-FFT and CP-FE at the higher triaxiality do not match as closely, as shown in Figure 4. The trends are consistent for the transverse strains, at least from the perspective of the ordering of the crystal orientations. The trends in growth rate, the focus of the current study, are consistent. Figure 4(c-d) shows that the transverse strains calculated by FFT and FEA differ significantly initially, by 2.5 times, but then eventually converge at higher plastic strains. At low strains, the transverse strains are going to be primarily due to the elastic strain contribution in the CP-FE. This large strain difference is also likely due to the difference in prescribed strain rate, since the specific strain rate prescribed in each method differs slightly (\dot{E}_{eq} in the DVP-FFT and \dot{E}_{33} in the CP-FE). The stress and volume fraction are within 20% between the corresponding CP-FE and DVP-FFT simulations. At both triaxialities, the void in the [111]-oriented crystal grows the fastest,

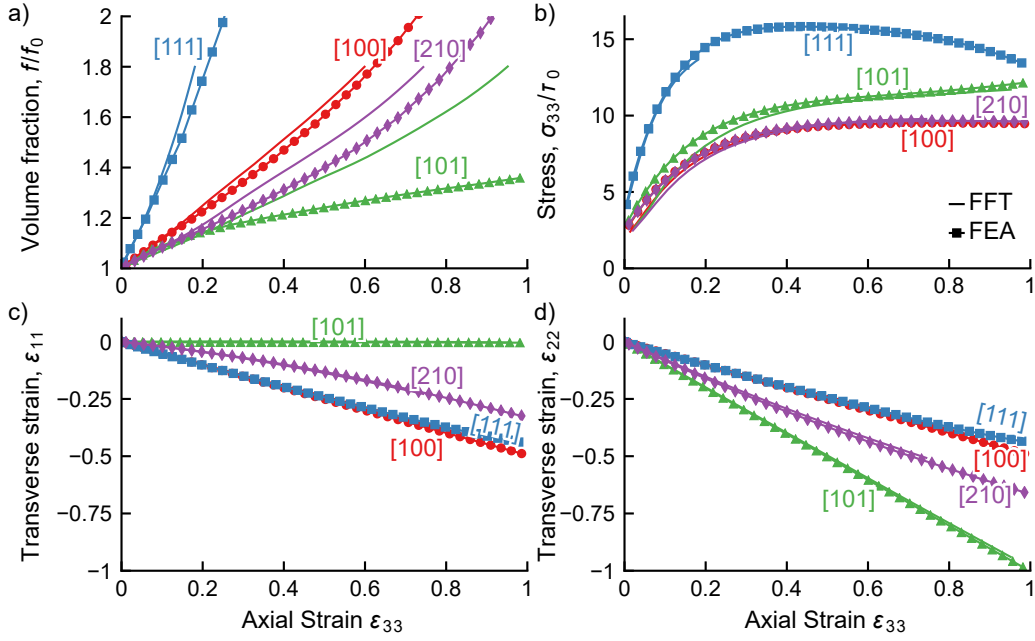


Figure 3: Figures comparing DVP-FFT (no symbols) and CP-FE (closed symbols) in single crystals at a low triaxiality ($T_X=0.6$). The figure (a) shows the volume fraction of the void, (b) axial stress, (c) transverse strains in the x direction, and (d) transverse strains in the y direction. The (b) stresses and (c, d) transverse strains in the material (to what extent the DVP-FFT completed) are within 10% of one another at strains above 20%, and the trends for the (a) volume fraction and, by extension, volume fraction rate, are consistent. At this low triaxiality, the voids in [111] and [101]-oriented crystals grow at the highest and lowest rate, respectively.

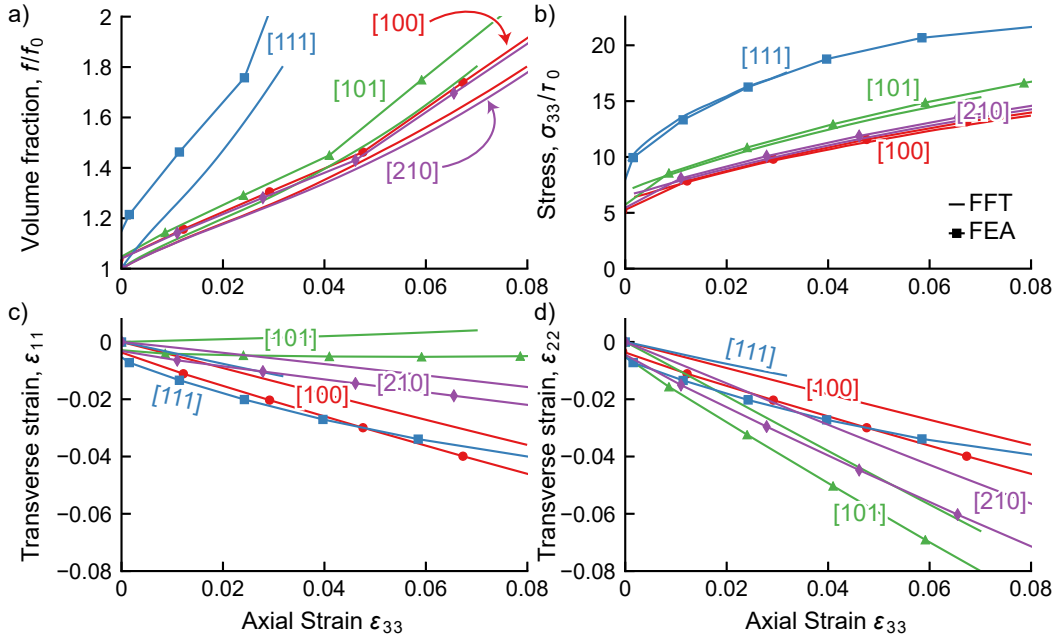


Figure 4: Figures comparing DVP-FFT (no symbols) and CP-FE (closed symbols) in single crystals at a high triaxiality ($T_X=3$). The figure (a) shows the volume fraction of the void, (b) axial stress, (c) in the x direction, and (d) transverse strains in the y direction. The DVP-FFT calculations complete a fraction of what the CP-FE completes. (a) The volume fractions are within 20% of each other between simulation types, and stresses differ by no more than 15% for each crystal orientation. Here, the (c, d) transverse strains differ significantly, but (a) both algorithms predict that the voids in the [100]-oriented grains grow the slowest, rather than the [101] grains. Both algorithms predict that the voids in the [111]-oriented grain grow fastest.

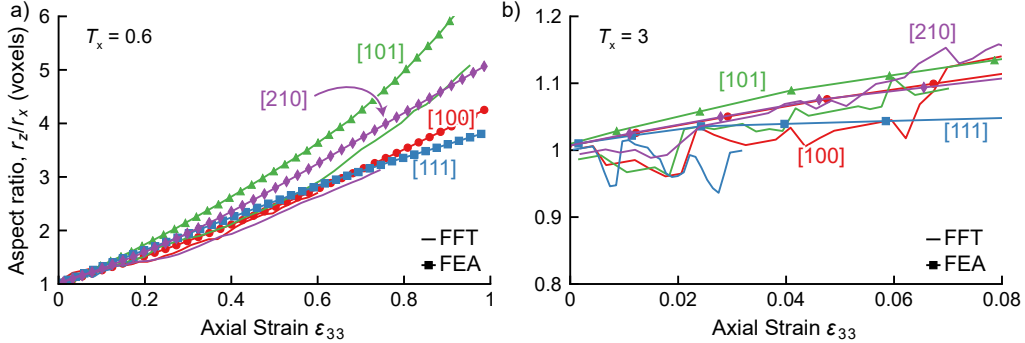


Figure 5: Figures showing aspect ratios vs the plastic macroscopic axial strain for both the DVP-FFT (no symbols) and CP-FE (closed symbols) in single crystals at (a) a low triaxiality ($T_X=0.6$) and (b) a high triaxiality ($T_X=3$). At both triaxialities, the DVP-FFT aspect ratio algorithm yielded more noise than that of the CP-FE. The aspect ratio of the voids in the (b) high triaxiality case in the DVP-FFT simulations exhibited significant noise, but both aspect ratios remain within 10% of the original value during the range shown.

while the void in the [101]-oriented crystal at the lower triaxiality and in the [100]-oriented crystal at higher triaxialities grows at the lowest rate. The DVP-FFT algorithm does not control the total axial strain, so the simulations at higher triaxialities use a much smaller time scale and maximum axial strain, to control the strain rate most accurately. Figure 3.1 shows the aspect ratio, AR , as a function of plastic strain in the axial direction, ϵ_{33}^p at the the lowest and highest triaxialities. The data contain some noise, since the post-processing aspect-ratio algorithm can encounter problems when the shape of the voids does not change significantly. At the higher triaxiality, with the least shape change, the noise is greatest, making comparison between the models difficult. Nonetheless, we clearly find that the aspect ratio at that triaxiality are within 20% between the corresponding CP-FE and DVP-FFT simulations. The Ling et al. [24] CP-FE results indicate the same trends in the cases of the [100], [101], and [100]-oriented crystals, but the void in the [210]-oriented crystals grew at a slower rate at both triaxialities reported [24], although they have a higher exponent ($n=15$) and the hardening rule differs. Other CP-FE simulations, such as those by Asim et al. [26] and Chen et al. [27] also show that soft grains appear to have faster void growth.

In summary, voids in FCC single crystals grow most rapidly in [111]-oriented crystals under strain-rate controlled conditions. This orientation

corresponds to plastically hard crystal relative to the loading direction. This is consistent across DVP-FFT and CP-FE, although slight variations between the two models exist, due to the fact that the CP-FE relies on a mesh and large-strain kinematics, while the DVP-FFT uses voxelized microstructures, as well as lacks the elastic behavior of the CP-FE. Because of the choice of a void volume fraction to both maximize observation and minimize interaction between voids, the trends seen here are expected to hold at lower porosity levels. This important conclusion of this comparison is that DVP-FFT yields comparable results with CP-FE and we can therefore rely on the more efficient DVP-FFT to investigate the relationship between crystal orientation and triaxiality on void growth with reliable statistics in polycrystals.

3.2. Voids in single crystals

The loading type dictate the void growth rate, as seen in figure 6, which shows the results of DVP-FFT simulations for voided single crystals with orientations [100], [101], and [111] with two sets of loading types: fully-stress controlled, and axial strain-rate controlled. In both cases, the stress triaxiality is controlled. When volume is plotted against strain, the void in the hard [111]-oriented crystal always grows at the highest rate. This trend was obtained for all strain-rate controlled simulations, but in the softest [100]-oriented crystals, porosity always grows the fastest in *time* with fully-imposed stress. When stress is fully imposed, the intermediate [101] orientation has the slowest void growth in time. Thus, depending on the local loading conditions, the apparent speed of void growth may reverse, which may account for experimental observations that voids are largest in soft grains [46].

Figure 7 shows the inverse pole figure (IPF) with a contour of the initial void growth rate with respect to strain for each single-crystal orientation represented in the IPF. Overall, the void growth rate in single crystals varies smoothly between any two of the three symmetric orientations ([100], [101], and [111]). The voids in all crystals experience an initial reduction, followed by an increase, in growth rate as the simulations progress (shown as a supplemental animation in the online version).

The calculations are repeated for a range of triaxialities, although not all are shown. For all triaxialities tested, the voids in [111]-oriented crystals grow the fastest with respect to strain. They continue to grow at the fastest rate for the entire straining period, including the initial reduction in growth rate. At low triaxialities, voids in [101]-oriented crystals grow the slowest, while at higher triaxialities, voids in [001]-oriented crystals grow the fastest,

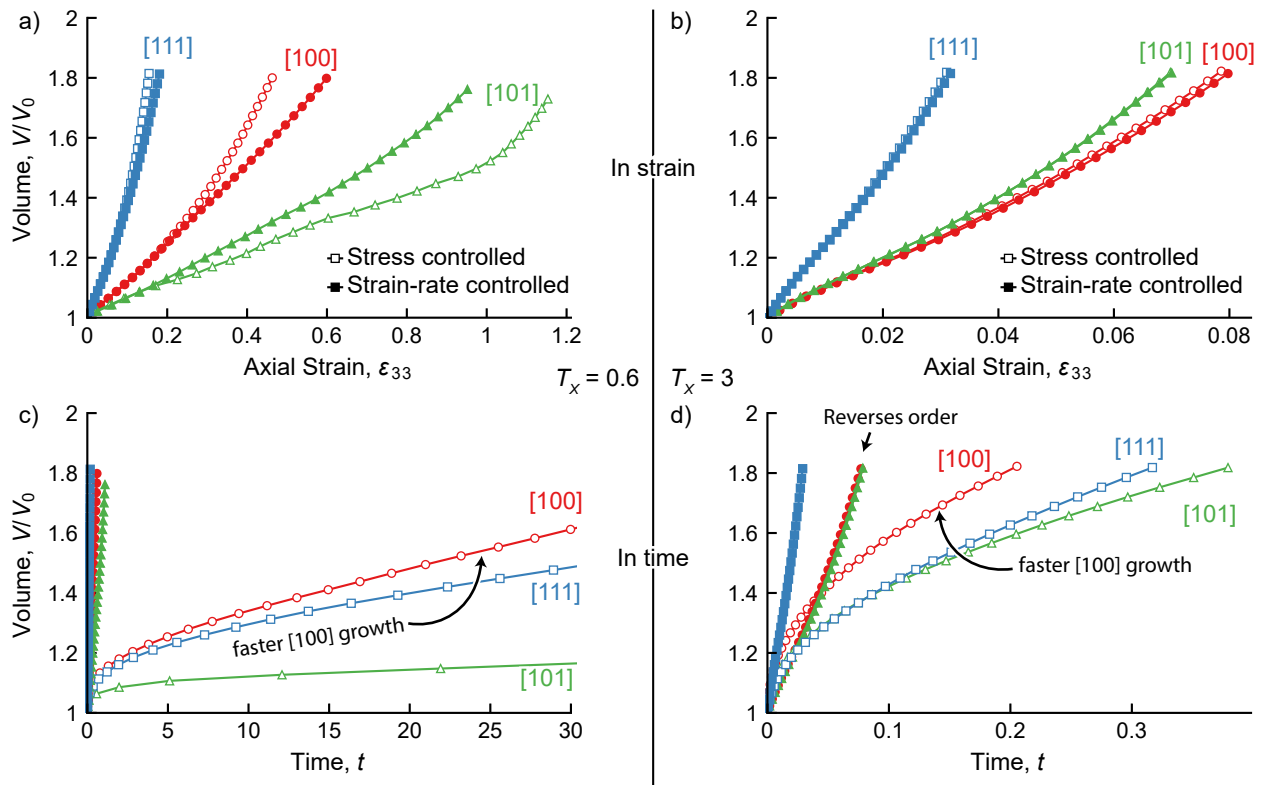


Figure 6: Volume vs axial strain and volume vs time plots for voids in single crystal voids in the DVP-FFT simulations at $T_x=0.6$ and $T_x=3$ show that loading types can reverse the order of growth rate in the single crystals. Under stress-controlled loading, the softest crystals grew fastest in *time*.

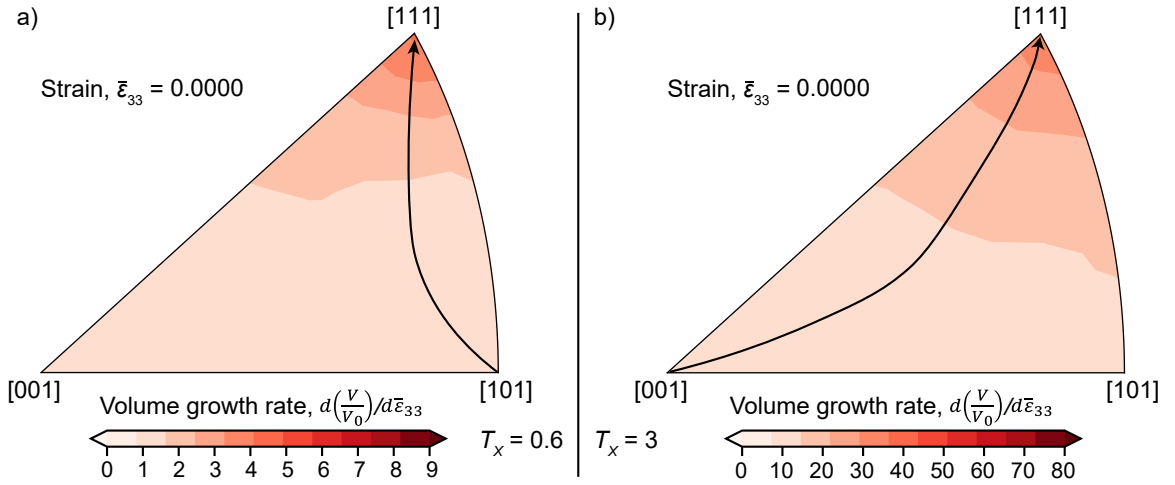


Figure 7: Initial volume growth rate (taken as the derivative of volume in terms of macroscopic axial plastic strain) as a function of orientation for single crystals at stress triaxiality (a) $T_x=0.6$ and (b) $T_x=3$. Each of the 72 points shown in Figure 2b is represented here by one individual simulation. The voids in the [111]-oriented single crystals grow fastest. At low triaxialities, the void in the [101]-oriented single crystal grows the slowest, while at higher triaxialities the void in the [100]-oriented crystal grows the slowest. The arrows are drawn to indicate the trend of fastest rate change, highlighting this shift between low and high triaxialities. The indicated trend was not numerically determined.

as is evident in figures 3 and 4. The arrow drawn in figure 7 illustrates the connection from the crystal orientation with the slowest-growing void to the orientation with the most rapidly growing void and approximately follows the path of the steepest gradient.

3.3. Voids in polycrystals

Next, we study void growth in fully voided polycrystals, in which every crystal has one starting intragranular void. In the 72-grain random structure, we expect that orientation effects on void growth to be highly variable and weak, in which much of the strong orientation effects on void growth seen in the isolated single crystals will be diminished.

In the 72-grain random case, each void has a different size and location in its parent crystal. In the 108-regular polycrystal, each void is the same size and centered inside its parent. The chief variable lies in the orientation of the surrounding grain neighbors. Voids in all neighboring grains will grow

at different rates and interact with one another. With these many sources of variation, we expect void growth across the polycrystal to be distributed. The question, however, concerns whether orientation effects on intragranular void growth seen in ideal single crystal tests are still preserved in a multiply-voided polycrystal.

Figure 8 shows IPF contour plots for polycrystals with the random 72-grain structure and the regular 108-grain structure. The IPFs represent the average of 30 realizations at the same macrostrain, plotted as a function of void growth rate with respect to strain vs. the crystal orientation containing each void. Since in the 72-grain polycrystal, each void is not the same size, the void volume was first normalized by its starting volume before averaging. Note that each point represents one of the 72 starting orientations. The additional randomly-generated orientations that supplemented the 108-grain polycrystal are not included in these plots to reduce clutter.

The strong correlation between orientation and void growth rate seen in the single crystals is diminished in the case of polycrystals, although the growth rate near the [111]-direction still remains consistently the highest for all triaxialities. At the lower triaxiality, both polycrystalline microstructures have a few other orientations with exceptionally high growth rates. In the random 72-grain polycrystals, these orientations are [327]-, [438]-, and [538], and in the regular 108-grain polycrystal, they are [219]- and [214]. At the higher triaxialities, the orientations with the highest growth rates are still exclusively the [111]-oriented crystals.

For both the single crystals and polycrystals, the growth rate varies non-monotonically with strain in a way that does not depend on its starting orientation. For voids in all single crystals, the growth rate varied in the same way, initially decreasing and then increasing with strain. The voids in the polycrystalline microstructures are not similar. In any individual simulation, the voids in some grains grow the fastest initially, only to slow down and be surpassed by other voids in grains with a different orientation.

To compare orientation effects with the single crystal cases, Figure 9 compares the volume of voids in selected starting orientations in the single crystals and the *average* volume of the voids in the corresponding crystal orientations in the polycrystalline microstructures.

The void growth in [111] grains in the polycrystals is, on average, slower than that of its single crystal counterpart. However, the orientation correlates more closely to growth at the highest triaxiality than for the lowest triaxiality, as is indicated in the Figure 8. It is possible that at even higher triaxialities,

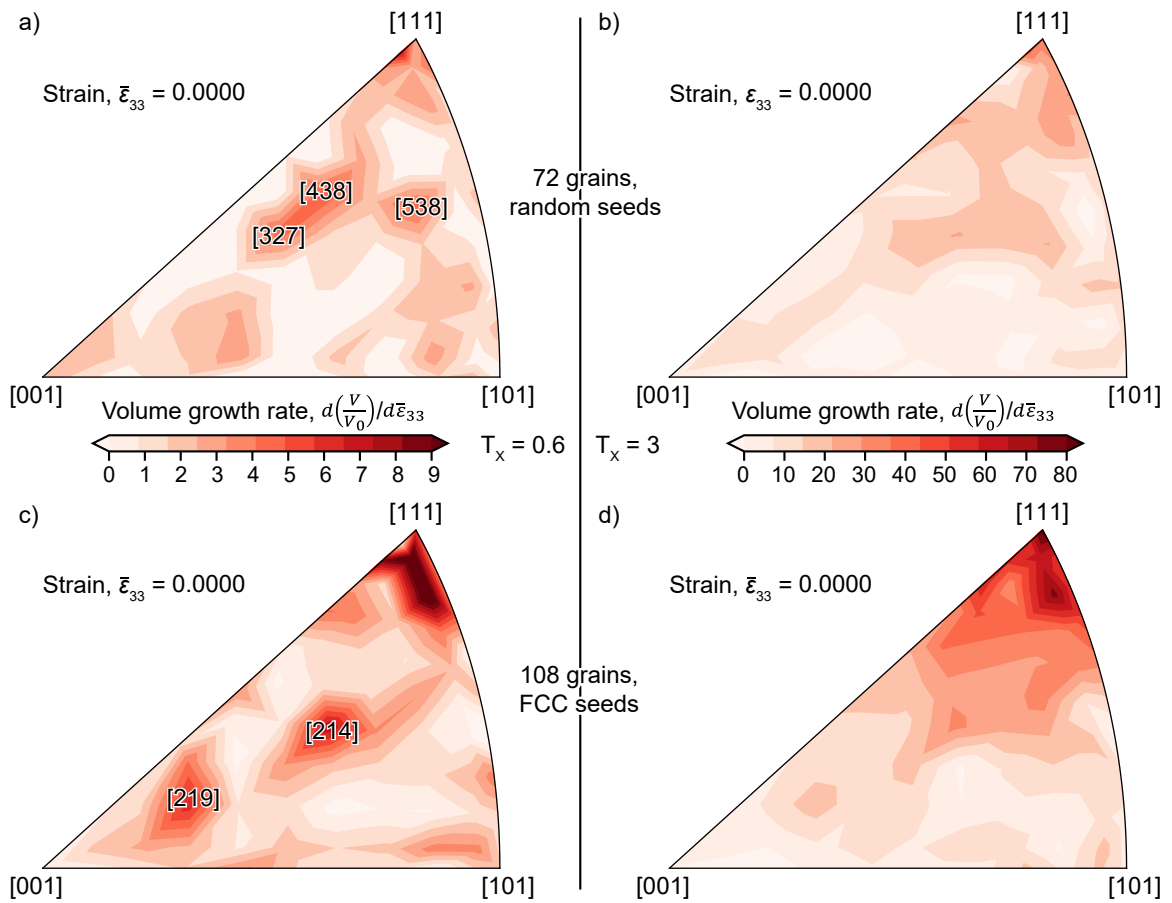


Figure 8: Initial volume growth rate (couched in terms of macroscopic axial plastic strain) as a function of orientation for polycrystals in the 72-grain polycrystal at a stress triaxiality of (a) $T_x=0.6$ and (b) $T_x=3$, and in the regular 108-grain polycrystal at a triaxiality of (c) $T_x=0.6$ and (d) $T_x=3$. The figures shown here represent the average of 30 realizations of polycrystals, plotted as a function of void growth rate vs containing crystal orientation (relative to the primary stress axis). Each of the 72 points shown in Figure 2b is represented here by the average of 30 simulations. The results are noisier than in single crystals, although voids grow consistently faster in grains oriented near the [111]-direction. The still does not capture the non-monotonic growth rate of the voids. See online version for animations.

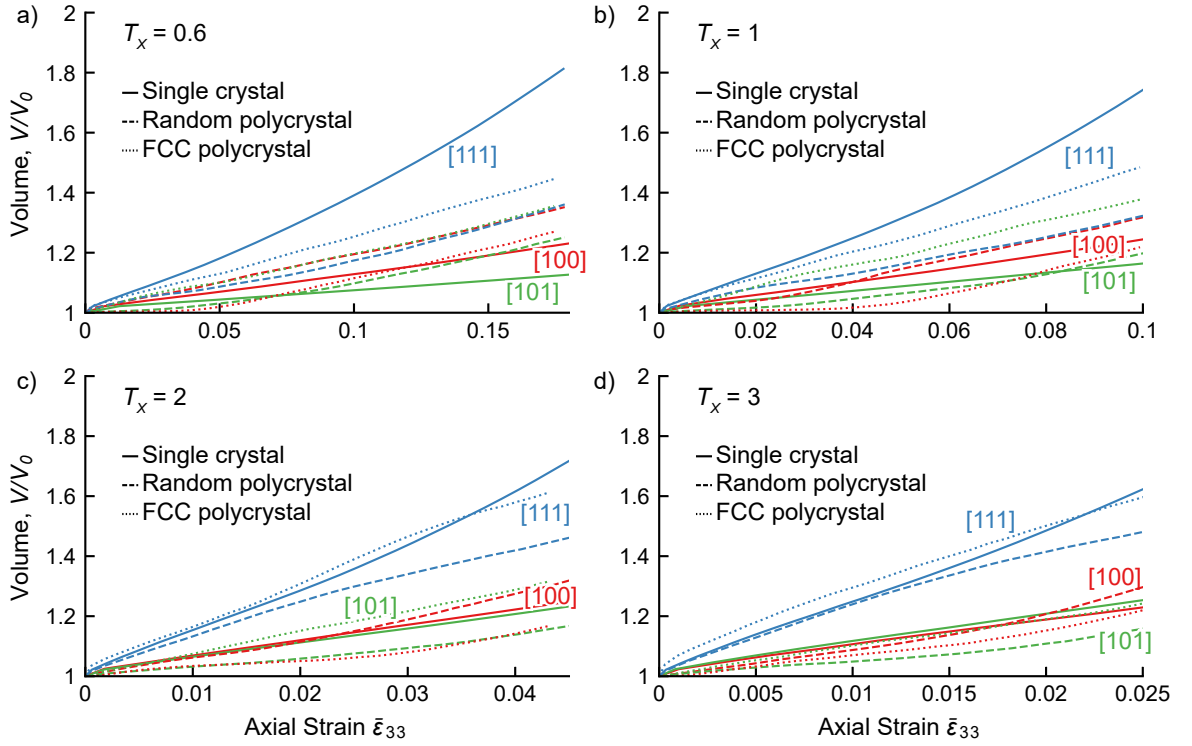


Figure 9: Volume vs axial strain plot for the corners of the stereographic figures, showing data analogous to the previous figures, for stress triaxialities (a) $T_x=0.6$, (b) $T_x =1$, (c) $T_x =2$, and (d) $T_x =3$. At every triaxiality, the void in a [111]-oriented single crystal grew the fastest. At low triaxialities, the void in the [101]-single crystal grew the slowest, but at higher triaxialities, the voids in the [101]-oriented crystals grow the slowest.

the voids in the [111]-oriented crystals in polycrystals would experience even greater growth.

In the 72-grain random polycrystals, for $T_X=3$, the voids in both the [111]- and [001]-oriented grains initially grow at similar rates to their single crystal counterpart. As the strain increases, the voids in the [001]-oriented grains in polycrystals appear to grow faster. Conversely, the voids in the [111]-oriented grains in polycrystals slow down as strain increases. This indicates that the [111] grains have reached a saturation stress, and that the [001] and [101] crystals continue to grow and compensate for this saturation. Overall, voids in [001]-oriented grains loaded with low stress triaxialities appear to grow faster, on average, in polycrystals than in a single crystal with the same orientation.

The voids loaded at low stress triaxialities appear to be the least sensitive to orientation in the 72-grain random polycrystal: the voids in the [111]-oriented grains grow at a similar average rate as the voids in the [001]-oriented grain. At high triaxialities, the voids grow faster in the [111] grains. Overall, the [101]-voids grew the slowest at all triaxialities.

The voids in the [001] grains have the most erratic behavior, having slow initial growth for $T_X=1$, but more moderate growth at the other triaxialities. The growth decreases to a minimum for $T_X=1$, and then increases towards its single crystal behavior for $T_X=3$. On average, these voids grow slower than their single-crystal (and, by extension, the 72-grain polycrystal). The voids in [101] grains grow faster in this ordered polycrystal at every triaxiality compared to the random polycrystal, but converges to the single crystal value at the highest triaxiality.

Based on observations from Lebensohn et al. [34], it has been proposed that the relationship between the parent orientation and growth rate seen in single crystals would reverse in polycrystals. It was seen in that work that the interconnecting material between two nearby voids experienced an increased plastic strain rate if the material was soft, such as an [001]-oriented grain. Accordingly, here, we would expect to see that while the voids in [111]-oriented crystals grow the fastest, the voids in the same orientations in polycrystal would grow the slowest. This appears to be the case at low triaxialities ($T_X=0.6$) but not at high triaxialities ($T_X=3$). The results here demonstrate that despite the interaction between two neighboring growing voids, at high triaxialities, the hardest crystals (i.e., [111]-oriented ones) continued to experience the most void growth.

Taken together the results on the fully voided polycrystals show that in-

tragranular void growth is insensitive to orientations at low triaxiality and very sensitive to orientations at high triaxiality. The strong propensity for growth in [111]-oriented crystals is reduced in polycrystals. Particularly at lower triaxialities, the material behaves more isotropically; that is, void growth is insensitive to parent orientation. In contrast, void growth correlates clearly with crystallography at high triaxialities. Like the single crystals, the parent orientations in the polycrystal that are not near the [111] orientation show reduced growth rates at higher triaxialities. The only exceptions to this are when the parent orientations have much lower growth rates than those of its immediate surrounding orientations.

3.4. Data spread and statistical significance

Figure 10 shows the mean void volume and one standard deviation away in the [111]- [101]-, and [001]-oriented crystals in Figure 8. The mean of each void tends to fall within the standard deviation of all three void types. The range of volume change is wide in polycrystals, bringing into question whether the number of realizations is sufficiently large to state that this variation is statistically significant. Yet, to date, to our knowledge, no report in the literature has completed such a study for polycrystals. Therefore, there is a need to take a closer look at the statistical significance of the differences in the obtained distributions and on the effect of grain neighborhood.

To determine the statistical significance of porosity distributions, the two-tailed p-value is determined for void volume at the same axial plastic strain between voids in [111]- [101]-, and [001]-oriented crystals, using the mean and standard deviation from Figure 10. When the p-value is close to unity, the two distributions are nearly identical. Any differences between the mean likely originate from rare cases or outliers. The low triaxiality simulation for the random polycrystal shown in the top left-hand corner in Figure 11 is one example. This is not the case at high triaxialities, wherein the void in the hardest crystal continued to experience the most growth.

When the value is close to zero (below the standard 5% threshold), the populations are statistically distinct from one another and any differences cannot be attributed to randomness. For instance, the p-value is less than 0.05 between the voids in [111]-oriented grains and both other grain orientations for the high triaxiality case in the regular 108-grain polycrystal. In other words, the voids in the [111]-oriented grains have void growth patterns that are distinct from the voids in both [101]- and [001]-oriented grains. The

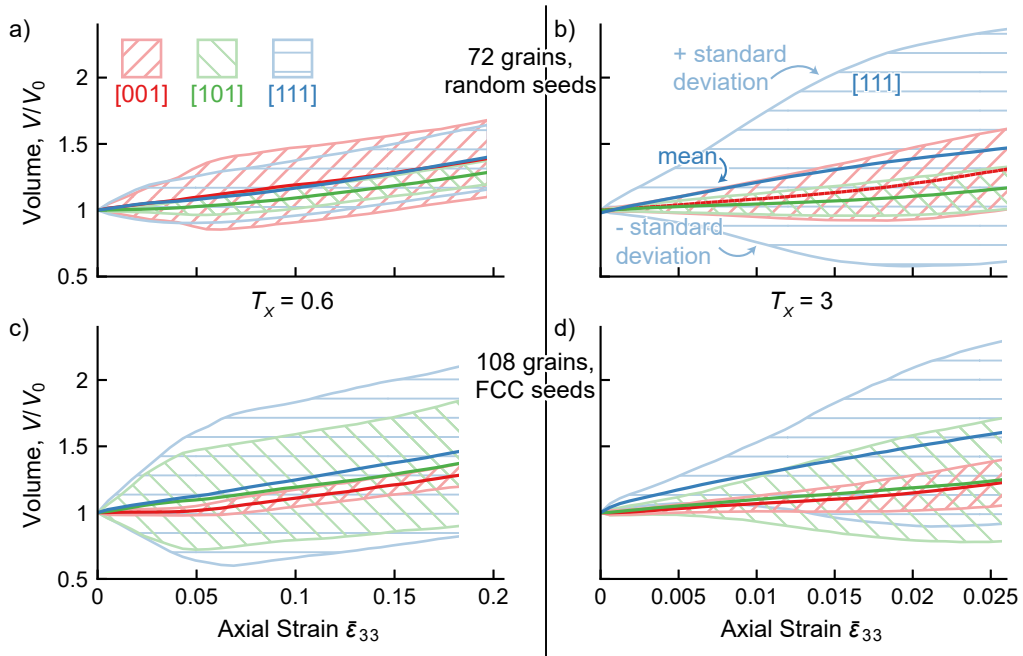


Figure 10: These figures show the mean (bold line) and one standard deviation bounds of void volume as a function of axial strain for the 72-grain polycrystal at a stress triaxiality of (a) $T_x=0.6$ and (b) $T_x=3$, and in the regular 108-grain polycrystal at a triaxiality of (c) $T_x=0.6$ and (d) $T_x=3$. What is most important to note is that the mean of the three directions falls within the standard deviation lines in every case. Note that the [111] case does have the greatest standard deviation in figures (b) and (c).

orientations of the parent grains are likely the primary cause of the faster void growth.

The other cases have intermediate p-values, well above the standard 5% threshold. At the lower triaxiality, and between the voids in [101]- and [001]-oriented grains at all triaxialities, the differences between the other two void populations are not statistically distinct. We suspect that in these cases, the faster void growth in the [101]-oriented grains is due more in part to the grain neighborhood than to the parent grain orientation.

3.5. Neighborhood effects

The spread in data in Figure 8 poses two important questions: to what extent is the spread due to neighborhood, and how is void growth affected by the Taylor Factor of the grains around the main grain that surrounds each void? To this end, a set of nine microstructures were designed to understand how longer-range average geometric hardness of the neighborhood affects the growth of the voids. These microstructures were created from existing microstructures to cover the possible extremes of the material. Each of these microstructures changed one of two aspects: either the hardness of the grain orientation containing a void or the average hardness of all the nearest neighboring grains of a central grain. These populations will be called interior grains and neighborhood grains, respectively, and in each case, only the growth of the void in the interior grain is tracked. Three interior grain orientations were chosen: soft, medium, and hard, shown as brown, green, and purple dots in Figure 12(b). For the neighborhood microstructures, three distinct microstructures among the 30 108-grain microstructures were randomly selected. The interior grain of interest was not touching the edges of the unit cell. The 12 neighbors were reassigned orientations lying in a similar location in orientation space, equally classified as either hard, med or soft, different from central grain. Figure 12 shows an example where the interior grain has a medium-hardness orientation, and the neighborhoods are either soft, medium, or hard, represented by the brown, *orange*, and purple grains, respectively. The other grains outside of this neighborhood retained their originally assigned orientations.

Figure 13 shows the strain evolution of the void growth in the central grain of each microstructure. Regardless of neighborhood, the hard interior grains have the fastest growth rate. For the same interior grain orientation, we observe that grains with hard neighborhoods grow faster than those with softer neighborhoods. At low triaxiality, the hardest level of the interior

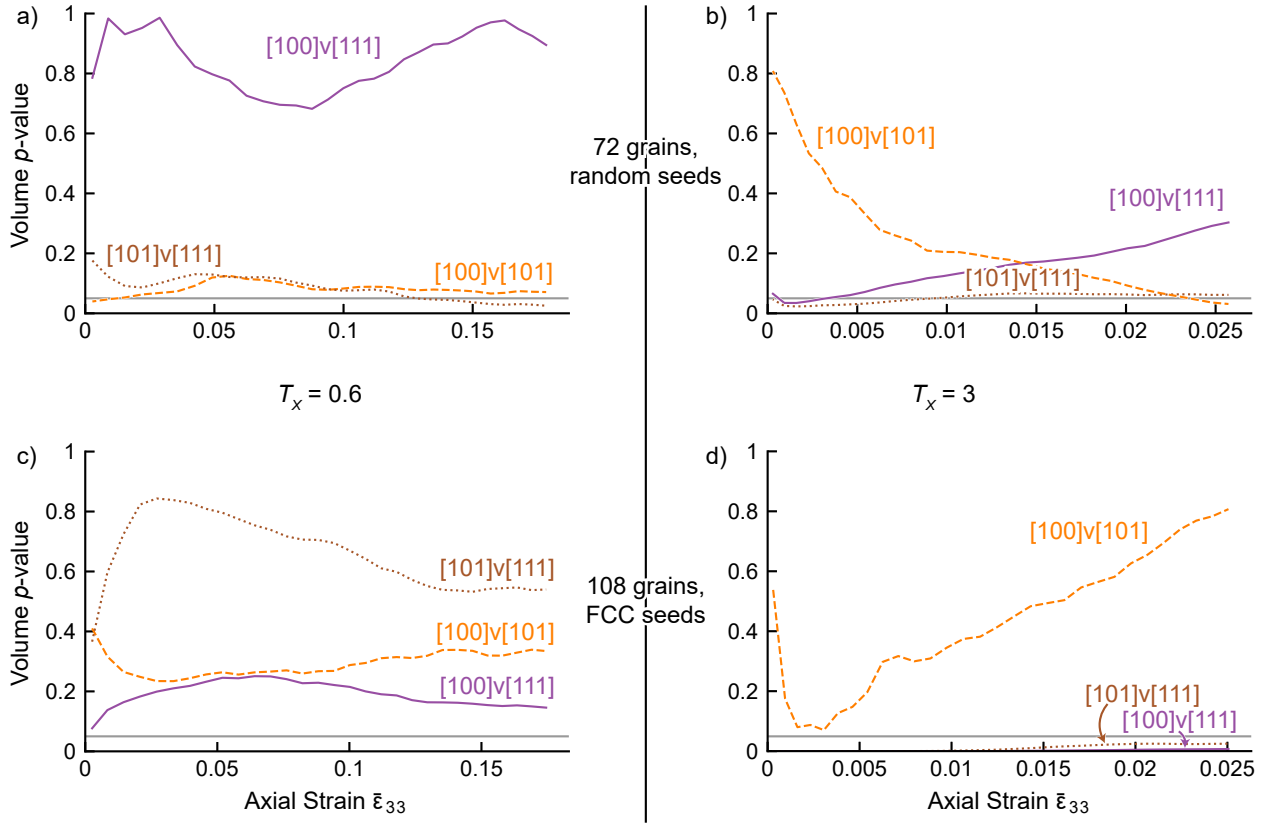


Figure 11: p -value plots based on the previous plots in figure 10, of the distribution of the void volume in the 72-grain polycrystal at a stress triaxiality of (a) $T_x=0.6$ and (b) $T_x=3$, and in the regular 108-grain polycrystal at a triaxiality of a stress triaxiality of (c) $T_x=0.6$ and (d) $T_x=3$. The orientations listed in the plot indicate the two grain populations compared. If a line is labeled, for example, $[100]v[111]$, each value compares the distribution of void volumes between voids in grains in $[100]$ -oriented grains and $[111]$ oriented grains at each axial strain. Note that only the voids in the $[111]$ are below a threshold of $\alpha < 0.05$ (which is a typical value) in figure (d), indicating that the $[111]$ population is distinct from the $[100]$ and $[101]$ -oriented populations.

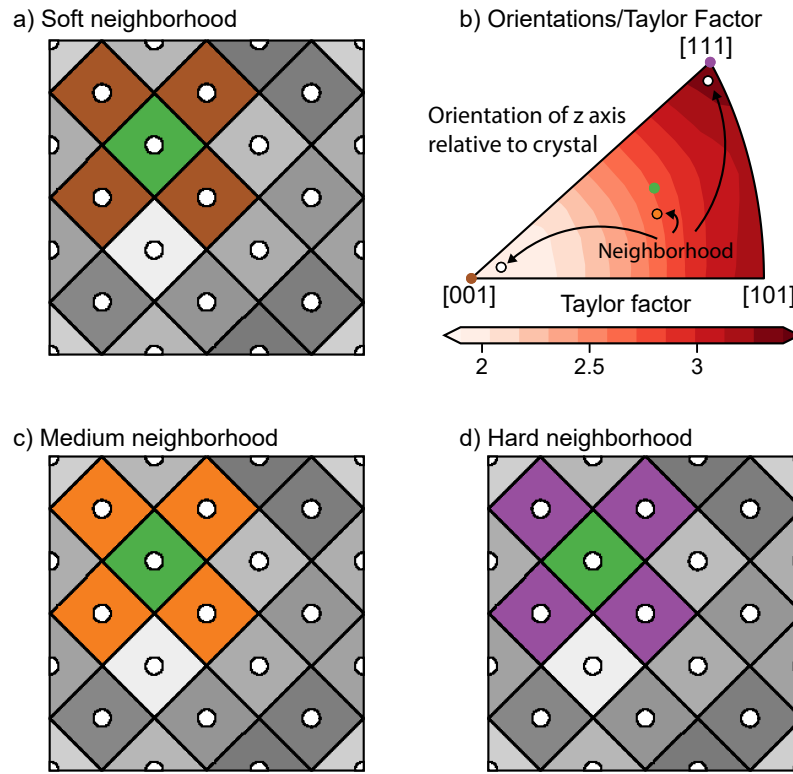


Figure 12: Simulations setup (a,c,d) for three of 9 of the neighborhood simulations, showing a medium interior grain (green), with a (a) soft, (c) medium, and (d) hard neighborhood. Note that there are 12 nearest neighbors in the 3D microstructure, and the medium orientation of the neighbors is not identical to the medium interior. Corresponding orientations can be seen in (b), where the additional outlined dots nearby the $[100]$ and $[111]$ orientation represent the orientations of the neighborhood when the interior grain has the closest orientation. In this case, the orange is closest to the green interior dot.

grain has less influence on void growth rate. We observe that both neighborhood and interior grain hardness level affect void growth rates, such that a medium hard interior grain with a medium neighborhood could grow slower than a soft interior grain with a hard neighborhood. This result identifies neighborhood as one source for the weakening influence of orientation on void growth within a polycrystal. At higher triaxiality, the effect of orientations can be more easily identified, wherein hard interior grains or hard neighborhoods would tend to increase growth rates. The apparent lack of growth, seen particularly in the soft grain with a soft neighborhood in Figure 13(b), is likely due to growth below the resolution of the voxelized Fourier grid. Faster growing grains are contributing to the macroscopic void growth, and thus the algorithm does not need to add additional void voxels to the Fourier grid. In Figure 13(c,d), we show the associated axial stresses versus strain curves. In all cases, the higher stresses generated in harder grains results in faster intragranular void growth rates. Neighborhood effects on stress states are not as influential as the orientation of the interior grain.

Grain neighborhoods likely made a difference in this analysis because changing 12 of the 108 grains can change the macroscopic stress. However, no major change in macroscopic stress occurred when the same orientations are simply reoriented, as in the original cases in section 3.3. However, we reveal a notable dependence of void growth on parent orientation. This implies that it is important to account for crystal orientation, particularly when the material is strongly textured or if stress concentrations tend to develop preferentially in particular orientations. Grain stress and its neighborhood Taylor factor are not strongly correlated at any triaxiality, but grain stress and its own Taylor factor is. Figure 14 shows the initial void growth speed of the void vs. the initial average grain stress for the original 30 108-grain simulations conducted, where each dot represents one grain in one of the 30 simulations and is colored by the Taylor factor of the grain. Again, we observe a correlation between the grain stress and its Taylor Factor at higher triaxiality, but not at low triaxiality.

The apparent insensitivity of growth rate to parent orientation seen in the lower triaxiality case was not seen in the single crystals and not seen in the polycrystal at high triaxiality. This difference points to a strong neighborhood effect. Considering that the orientation plays a smaller role when approaching hydrostatic loading, this trend is unexpected. One possibility is that the load in the grains is sufficiently directional, but the neighborhood behavior approaches an isotropic medium, reducing the neighborhood effect,

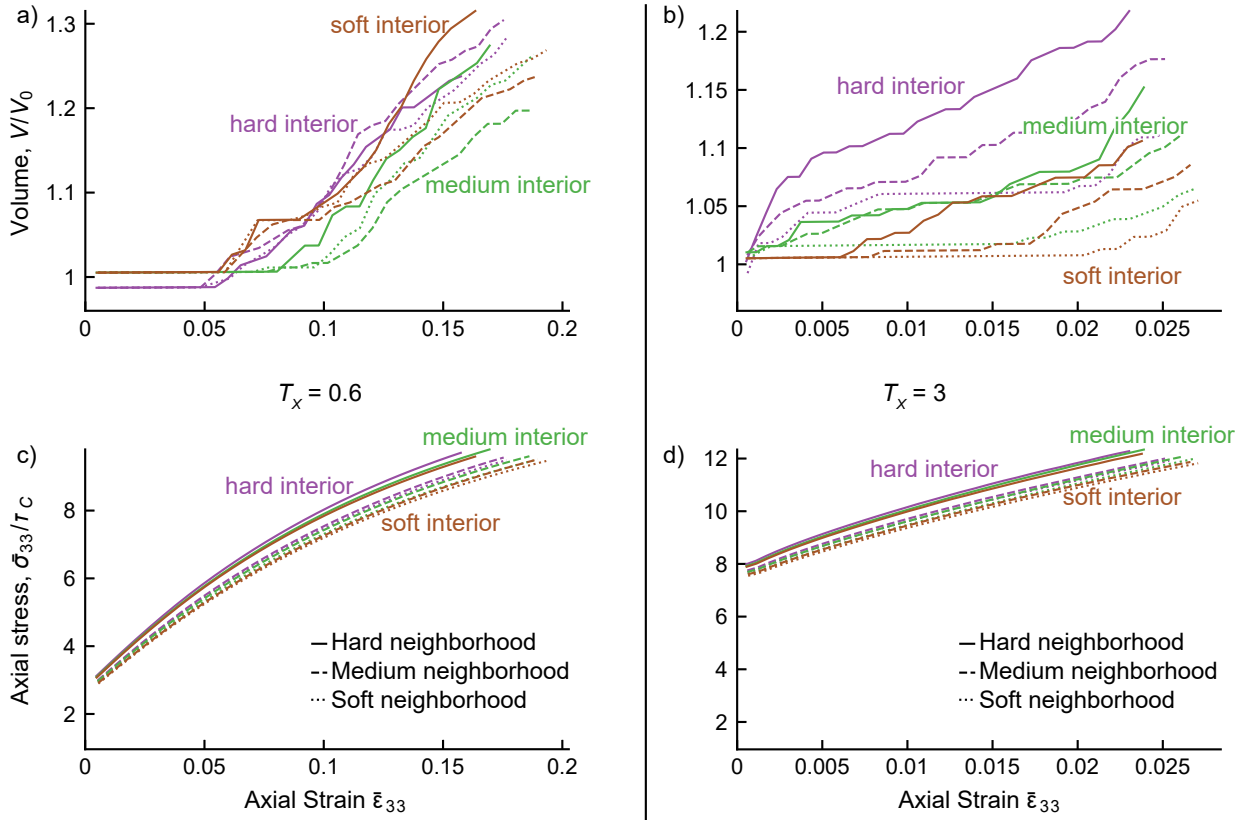


Figure 13: Volume vs strain (a,b) and macroscopic stress vs strain (c,d) plots of voids in the regular polycrystals at two triaxialities (a,c) $T_x=0.6$ and (b,d) $T_x=3$, where the voids are inside a hard, medium, or soft grain (purple, green, and brown, as labeled as the interior grain), where the grains nearest neighbors are all hard, medium, or soft (solid, dashed, or dotted). These plots correspond to microstructures detailed in figure 12. The plots reveal that the hardest grains (and interiors) have the most void growth.

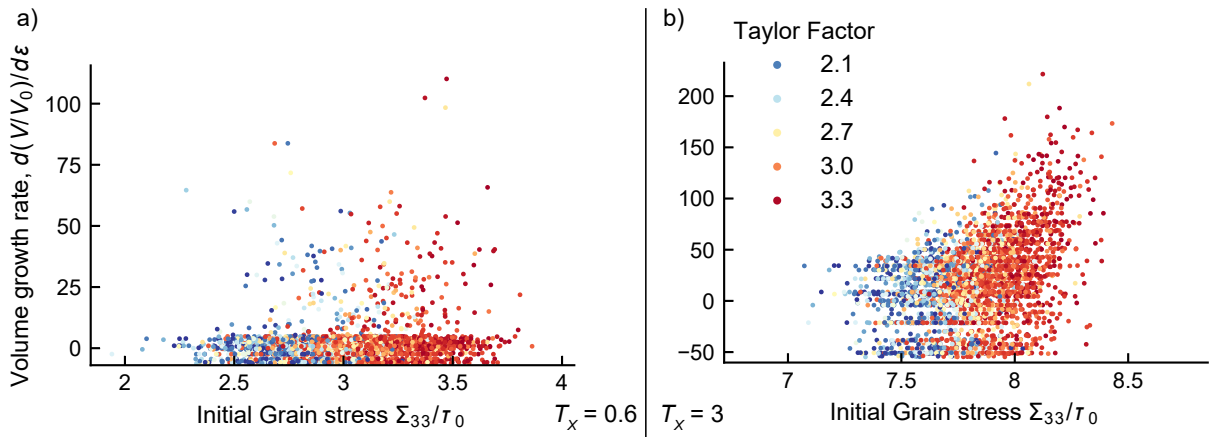


Figure 14: Initial void growth velocity vs stress (with dots colored by Taylor factor) for all 30 realizations of the regular FCC super-lattice grain structure with 108 grains at stress triaxialities of (a) $T_x=0.6$ and (b) 3. The figures indicate that grain stress correlates with Taylor Factor, but only at the higher triaxiality is there any appreciable increase in void growth velocity with grain stress.

and in consequence allowing the anisotropic response of each grain. On the other hand, when the grain is loaded in nearly uniaxial tension, the anisotropy of the neighborhood is amplified, which in turn may shield individual grains.

The relevance and novelty of this work, in terms of unraveling the dependence of intragranular void growth with microstructural (e.g. grain orientation and grain neighborhood effects) and mechanical features (e.g. triaxiality), should be considered in connection with recent state-of-art in-situ characterization experiments, as well as a potential guidance for the design of forthcoming experiments of this kind. In-situ characterization of damage in engineering alloys, like the void-tracking experiments based on 3-D X-ray micro-tomography, mentioned in the introduction as motivation for the present study [1, 2], revealed a significant dispersion of void growth, qualitatively consistent with our results. However, a more quantitative comparison and cross-validation between experiments and predictions would require not one but two simultaneous in-situ characterization methods to identify void's and grain's spatial locations, as well as grain orientations. Recent multimodal experiments with this level of fidelity have been reported in the literature, but not necessarily for the in-situ characterization of engineering alloys fabricated using standard processing techniques. For example, Lieberman et al. [47] pre-characterized ex-situ the local orientation field using 3-D High-

Energy Diffraction Microscopy (HEDM) in a high-purity copper sample. The sample was then incipiently spalled and post-characterized in terms of its void distribution, providing confirmation of damage occurred primarily by voids forming at grain boundaries. With this data, the post-mortem correlation between voids, grain orientations and grain boundary types was subsequently analyzed using FFT-based methods. Pokharel et al. [48] used tomography and orientation mapping to study a 2-phase metal-metal composite, in which damage mainly occurs by debonding between phases. Naragani et al. [49] used similar characterization techniques to study damage/orientation correlations, including at the void coalescence stage, in an additively manufactured Ni superalloy, in which relatively large voids (with respect to the grain size) were printed, i.e. pre-seeded in the microstructure. These recent multi-modal experiments demonstrate that these state-of-the-art techniques are mature enough to deliver data to contrast with our model results. The predictions reported in this paper should be provide guidance to experimentalists on where to look next.

Specifically, we envision that, depending on the loading conditions, the texture could affect the macroscopic behavior of the material, but at a microscopic level, the voids behave as if they were in a more isotropic medium. That is to say, in low-triaxiality simulations, we found no strong isotropy in polycrystals, where single crystal behavior differs more significantly. At higher triaxialities (and more dynamic loads), the opposite would be thus expected: macroscopically, the material would behave more isotropically, but the voids would grow heterogeneously on average, i.e. fastest/slowest in the hardest-oriented grains for displacement-rate/load controlled experiments, which could cause different coalescence behavior and thus failure. As there are no such experiments yet available that directly compared the void growth rate in polycrystals, our results suggest the design of new experiments in engineering materials to look into the average growth rate of voids of various orientations, for cross-validation with the model predictions.

4. Conclusions

In this work, using a dilatational visco-plasticity fast Fourier transform-based model, we investigated crystallographic orientation effects on the growth of intragranular voids. Without the effects of void nucleation and coalescence, three sets of simulations with different crystalline microstructures were conducted, and the orientations of the grains in these microstructures were varied

over the full orientation space. The first type of microstructures were single crystals, the second type, Voronoi polycrystals where every grain had one void in its interior, and the third type, another voided polycrystal where the void centers were the centers of a FCC super-lattice with 12 nearest neighbors, and the grains filled the Wigner-Seitz cells surrounding them. In each case, the initial void volume fraction per grain is 1%. A set of 72 orientations were tested for the single crystal, and those same 72 orientations were applied to 30 random realizations of both of types of polycrystals, so that the neighborhood (and, in the case of the random polycrystal, the grain morphology) was different in each realization. Each of these microstructures were simulated at four axisymmetric triaxialities, to determine if triaxiality had an effect on the void growth. For some select cases, DVP-FFT and CP-FE models were conducted on nearly the same microstructures. The comparison demonstrated that DVP-FFT yields comparable results with CP-FE.

The trends are clear in single crystals; the voids in the $[111]$ -oriented grains, that is in the hardest grain, grow the fastest in strain-rate-controlled simulations. At lower triaxialities, the void growth rate is slower overall, and the voids in the $[101]$ -oriented grains grow the slowest. At higher triaxialities, the void growth is much more rapid, and the slowest growing void is the void in the $[101]$ -oriented grain. In simulations where the stress was fully prescribed, the slowest growing voids were the $[101]$ -oriented grains, and the softest grain had the fastest voids growth. The void growth rate with respect to strain is identical to the constant-strain-rate simulations.

In polycrystals, not only the grain orientation, but also the nearest grain neighborhood plays a large role in dictating the void growth, especially at lower triaxialities. At higher triaxialities, most notably in the regular polycrystal, the single crystal trend become more apparent and the voids in the $[111]$ -oriented grains grow the fastest on average.

In the case of the polycrystals, it was unexpected that the fastest growing void is the intragranular void in the hardest grain. This outcome contradicted previous observations for a different configuration (i.e. intergranular porosity) that the voids would grow the fastest in the softest grain, given that soft single-crystal ligaments between intergranular voids in polycrystals can deform at higher strain rate under the same stress [34]. The expectation was that by surrounding the void with a soft material in a heterogeneous polycrystal, the soft material would deform plastically the fastest. This would result in faster void growth, since dilatational plasticity models are predicated on the idea that the deformation of the surrounding material deter-

mines void growth. The findings of this work suggest that crystal orientation has a significant influence on the growth of voids it contains. They imply that crystal orientation needs to be considered in the response of polycrystalline materials, particularly those that have texture or in which local stress concentrations preferentially develop in certain orientations.

This study did not identify any clear trends in the role of the neighborhood in the growth of voids, neither due to void neighborhood hardness nor hardness disparity, but did suggest that neighborhood can affect the void growth if it increases or decreases the stress of the grain, particularly at high triaxialities. In addition, it would appear that the neighborhood plays a strong role in reducing the expected anisotropic behavior at low triaxialities. It appears, also, that at higher triaxialities, the neighborhood does not play as strong a role, because grain stress, Taylor factor, and void growth rate correlate more strongly. Determining to what extent the neighborhood plays a role would be an interesting and important study in the future. Given that, for example, in high-purity metals voids typically form at grain boundaries and junctions, it is also imperative to study the effect of growth at grain boundaries and triple junctions, as the neighborhood effects are expected to play a more complex role.

The polycrystalline results indicate a discrepancy in isotropic behavior between macroscopic and microscopic properties, pointing to trends that might be observable in future experiments. In low-triaxiality simulations, the texture is expected to dominate the macroscopic properties, but not the void growth rate in randomly-textured samples. At higher triaxialities, while the sample might behave more isotropically, the voids may grow at different rates in relation to containing grain's crystal orientation. New in-situ experiments on engineering materials may need to track void growth of intragranular voids and compare the void growth rate at different triaxialities and with different loading conditions.

5. Acknowledgements

This material is based upon work supported by the Department of Energy, National Nuclear Security Administration under Award No. DE-NA0003857. The authors would also thank Pr. Laurent Delannay (UCLouvain, Belgium) for providing the FE crystal plasticity subroutine. RAL acknowledges support from Los Alamos National Laboratory's Science Campaign 2 and JMP program.

References

- [1] L. Lecarme, E. Maire, A. Kumar K.C., C. De Vleeschouwer, L. Jacques, A. Simar, T. Pardoen, Heterogenous void growth revealed by in situ 3-D X-ray microtomography using automatic cavity tracking, *Acta Materialia* 63 (2014) 130–139. URL: <http://linkinghub.elsevier.com/retrieve/pii/S1359645413007659>. doi:10.1016/j.actamat.2013.10.014.
- [2] F. Hannard, T. Pardoen, E. Maire, C. Le Bourlot, R. Mokso, A. Simar, Characterization and micromechanical modelling of microstructural heterogeneity effects on ductile fracture of 6xxx aluminium alloys, *Acta Materialia* 103 (2016) 558–572. URL: <http://linkinghub.elsevier.com/retrieve/pii/S1359645415300094>. doi:10.1016/j.actamat.2015.10.008.
- [3] S. H. Goods, L. M. Brown, Overview No. 1. The nucleation of cavities by plastic deformation, *Acta Metallurgica* 27 (1979) 1–15. doi:10.1016/0001-6160(79)90051-8.
- [4] F. Roters, P. Eisenlohr, L. Hantcherli, D. D. Tjahjanto, T. R. Bieler, D. Raabe, Overview of constitutive laws, kinematics, homogenization and multiscale methods in crystal plasticity finite-element modeling: Theory, experiments, applications, *Acta Materialia* 58 (2010) 1152–1211. doi:10.1016/j.actamat.2009.10.058.
- [5] R. A. Lebensohn, N-site modeling of a 3D viscoplastic polycrystal using Fast Fourier Transform, *Acta Materialia* 49 (2001) 2723–2737. doi:10.1016/S1359-6454(01)00172-0.
- [6] R. A. Lebensohn, R. Brenner, O. Castelnau, A. D. Rollett, Orientation image-based micromechanical modelling of subgrain texture evolution in polycrystalline copper, *Acta Materialia* 56 (2008) 3914–3926. doi:10.1016/j.actamat.2008.04.016.
- [7] R. A. Lebensohn, A. K. Kanjarla, P. Eisenlohr, An elasto-viscoplastic formulation based on fast Fourier transforms for the prediction of micromechanical fields in polycrystalline materials, *International Journal of Plasticity* 32-33 (2012) 59–69. doi:10.1016/j.ijplas.2011.12.005.

- [8] P. Eisenlohr, M. Diehl, R. A. Lebensohn, F. Roters, A spectral method solution to crystal elasto-viscoplasticity at finite strains, *International Journal of Plasticity* 46 (2013) 37–53. doi:10.1016/j.ijplas.2012.09.012.
- [9] J. R. Rice, D. M. Tracey, On the ductile enlargement of voids in triaxial stress fields*, *Journal of the Mechanics and Physics of Solids* 17 (1969) 201–217. doi:10.1016/0022-5096(69)90033-7.
- [10] A. L. Gurson, Continuum Theory of Ductile Rupture by Void Nucleation and Growth: Part I—Yield Criteria and Flow Rules for Porous Ductile Media, *Journal of Engineering Materials and Technology* 99 (1977) 2–15. URL: <http://MaterialsTechnology.asmedigitalcollection.asme.org/article.aspx?articleid=1422194>. doi:10.1115/1.3443401.
- [11] V. Tvergaard, A. Needleman, Analysis of the cup-cone fracture in a round tensile bar, *Acta Metallurgica* 32 (1984) 157–169. doi:10.1016/0001-6160(84)90213-X.
- [12] J. B. Leblond, G. Perrin, P. Suquet, Exact results and approximate models for porous viscoplastic solids, *International Journal of Plasticity* 10 (1994) 213–235. doi:10.1016/0749-6419(94)90001-9.
- [13] M. Gologanu, J. B. Leblond, J. Devaux, Approximate models for ductile metals containing nonspherioal voids-case of axisymmetric oblate ellipsoidal cavities, *Journal of Engineering Materials and Technology, Transactions of the ASME* 116 (1994) 290–297. URL: http://asmedigitalcollection.asme.org/materialstechnology/article-pdf/116/3/290/5516590/290_1.pdf. doi:10.1115/1.2904290.
- [14] M. Gărăjeu, J. C. Michel, P. Suquet, A micromechanical approach of damage in viscoplastic materials by evolution in size, shape and distribution of voids, *Computer Methods in Applied Mechanics and Engineering* 183 (2000) 223–246. doi:10.1016/S0045-7825(99)00220-0.
- [15] A. A. Benzerga, J. Besson, Plastic potentials for anisotropic porous solids, *European Journal of Mechanics, A/Solids* 20 (2001) 397–434. doi:10.1016/S0997-7538(01)01147-0.

- [16] V. Monchiet, O. Cazacu, E. Charkaluk, D. Kondo, Macroscopic yield criteria for plastic anisotropic materials containing spheroidal voids, *International Journal of Plasticity* 24 (2008) 1158–1189. doi:10.1016/j.ijplas.2007.08.008.
- [17] O. Cazacu, J. B. Stewart, Analytic plastic potential for porous aggregates with matrix exhibiting tension-compression asymmetry, *Journal of the Mechanics and Physics of Solids* 57 (2009) 325–341. doi:10.1016/j.jmps.2008.10.010.
- [18] J. B. Stewart, O. Cazacu, Analytical yield criterion for an anisotropic material containing spherical voids and exhibiting tension-compression asymmetry, *International Journal of Solids and Structures* 48 (2011) 357–373. doi:10.1016/j.ijsolstr.2010.10.009.
- [19] K. Danas, M. I. Idiart, P. P. Castañeda, A homogenization-based constitutive model for isotropic viscoplastic porous media, *International Journal of Solids and Structures* 45 (2008) 3392–3409. doi:10.1016/j.ijsolstr.2008.02.007.
- [20] A. Mbiakop, A. Constantinescu, K. Danas, An analytical model for porous single crystals with ellipsoidal voids, *Journal of the Mechanics and Physics of Solids* 84 (2015) 436–467. doi:10.1016/j.jmps.2015.07.011.
- [21] S. K. Yerra, C. Tekoğlu, F. Scheyvaerts, L. Delannay, P. Van Houtte, T. Pardoen, Void growth and coalescence in single crystals, *International Journal of Solids and Structures* 47 (2010) 1016–1029. doi:10.1016/j.ijsolstr.2009.12.019.
- [22] X. Han, J. Besson, S. Forest, B. Tanguy, S. Bugat, A yield function for single crystals containing voids, *International Journal of Solids and Structures* 50 (2013) 2115–2131. doi:10.1016/j.ijsolstr.2013.02.005.
- [23] A. Srivastava, A. Needleman, Effect of crystal orientation on porosity evolution in a creeping single crystal, *Mechanics of Materials* 90 (2015) 10–29. doi:10.1016/j.mechmat.2015.01.015.
- [24] C. Ling, J. Besson, S. Forest, B. Tanguy, F. Latourte, E. Bosso, An elastoviscoplastic model for porous single crystals at finite strains and

- its assessment based on unit cell simulations, *International Journal of Plasticity* 84 (2016) 58–87. doi:10.1016/j.ijplas.2016.05.001.
- [25] H. J. Guo, C. Ling, E. P. Busso, Z. Zhong, D. F. Li, Crystal plasticity based investigation of micro-void evolution under multi-axial loading conditions, *International Journal of Plasticity* 129 (2020) 102673. doi:10.1016/j.ijplas.2020.102673.
- [26] U. B. Asim, M. A. Siddiq, M. E. Kartal, A CPFEM based study to understand the void growth in high strength dual-phase titanium alloy (Ti-10V-2Fe-3Al), *International Journal of Plasticity* 122 (2019) 188–211. doi:10.1016/j.ijplas.2019.07.002.
- [27] T. Chen, R. Sakidja, W. Y. Ching, C. Zhou, Crystal Plasticity Modeling of Void Growth on Grain Boundaries in Ni-Based Superalloys, *JOM* 71 (2019) 3859–3868. URL: <https://doi.org/10.1007/s11837-019-03694-3>. doi:10.1007/s11837-019-03694-3.
- [28] J. Liu, M. Huang, Z. Li, L. Zhao, Y. Zhu, Microvoid growth mechanism in FCC polycrystals and a statistical damage model, *International Journal of Plasticity* 137 (2021) 102888. doi:10.1016/j.ijplas.2020.102888.
- [29] F. Fritzen, S. Forest, T. Böhlke, D. Kondo, T. Kanit, Computational homogenization of elasto-plastic porous metals, *International Journal of Plasticity* 29 (2012) 102–119. doi:10.1016/j.ijplas.2011.08.005.
- [30] A. Needleman, V. Tvergaard, An analysis of ductile rupture modes at a crack tip, *Journal of the Mechanics and Physics of Solids* 35 (1987) 151–183. doi:10.1016/0022-5096(87)90034-2.
- [31] S. Ghosh, J. Bai, D. Paquet, Homogenization-based continuum plasticity-damage model for ductile failure of materials containing heterogeneities, *Journal of the Mechanics and Physics of Solids* 57 (2009) 1017–1044. doi:10.1016/j.jmps.2009.04.002.
- [32] N. Bilger, F. Auslender, M. Bornert, J. C. Michel, H. Moulinec, P. Suquet, A. Zaoui, Effect of a nonuniform distribution of voids on the plastic response of voided materials: A computational and statistical analysis, in: *International Journal of Solids and Structures*, volume 42, Elsevier Ltd, 2005, pp. 517–538. doi:10.1016/j.ijsolstr.2004.06.048.

- [33] N. Bilger, F. Auslender, M. Bornert, H. Moulinec, A. Zaoui, Bounds and estimates for the effective yield surface of porous media with a uniform or a nonuniform distribution of voids, *European Journal of Mechanics, A/Solids* 26 (2007) 810–836. doi:10.1016/j.euromechsol.2007.01.004.
- [34] R. Lebensohn, M. Idiart, P. P. Castañeda, P.-G. Vincent, Dilational viscoplasticity of polycrystalline solids with intergranular cavities, *Philosophical Magazine* 91 (2011) 3038–3067. URL: <http://www.tandfonline.com/doi/abs/10.1080/14786435.2011.561811>. doi:10.1080/14786435.2011.561811.
- [35] P. G. Vincent, P. Suquet, Y. Monerie, H. Moulinec, Effective flow surface of porous materials with two populations of voids under internal pressure: II. Full-field simulations, *International Journal of Plasticity* 56 (2014) 74–98. doi:10.1016/j.ijplas.2013.11.012.
- [36] R. A. Lebensohn, J. P. Escobedo, E. K. Cerreta, D. Dennis-Koller, C. A. Bronkhorst, J. F. Bingert, Modeling void growth in polycrystalline materials, *Acta Materialia* 61 (2013) 6918–6932. doi:10.1016/j.actamat.2013.08.004.
- [37] D. Sulsky, H. L. Schreyer, Axisymmetric form of the material point method with applications to upsetting and Taylor impact problems, *Computer Methods in Applied Mechanics and Engineering* 139 (1996) 409–429. doi:10.1016/S0045-7825(96)01091-2.
- [38] N. Lahellec, J. C. Michel, H. Moulinec, P. Suquet, Analysis of Inhomogeneous Materials at Large Strains using Fast Fourier Transforms, in: C. Miehe (Ed.), *IUTAM Symposium on Computational Mechanics of Solid Materials at Large Strains*, Dordrecht: Kluwer Academic, Stuttgart, Germany, 2001, pp. 247–258.
- [39] C. Tomé, G. R. Canova, U. F. Kocks, N. Christodoulou, J. J. Jonas, The relation between macroscopic and microscopic strain hardening in F.C.C. polycrystals, *Acta Metallurgica* 32 (1984) 1637–1653. doi:10.1016/0001-6160(84)90222-0.
- [40] J. C. Michel, H. Moulinec, P. Suquet, A computational method based on augmented lagrangians and fast fourier transforms for composites with

high contrast, CMES - Computer Modeling in Engineering and Sciences 1 (2000) 79–88. doi:10.3970/cmes.2000.001.239.

- [41] V. Tvergaard, Influence of voids on shear band instabilities under plane strain conditions, *International Journal of Fracture* 17 (1981) 389–407. URL: <https://link.springer.com/article/10.1007/BF00036191>. doi:10.1007/BF00036191.
- [42] L. Delannay, P. J. Jacques, S. R. Kalidindi, Finite element modeling of crystal plasticity with grains shaped as truncated octahedrons, *International Journal of Plasticity* 22 (2006) 1879–1898. doi:10.1016/j.ijplas.2006.01.008.
- [43] S. Dancette, L. Delannay, K. Renard, M. A. Melchior, P. J. Jacques, Crystal plasticity modeling of texture development and hardening in TWIP steels, *Acta Materialia* 60 (2012) 2135–2145. doi:10.1016/j.actamat.2012.01.015.
- [44] L. Lecarme, C. Tekoğlu, T. Pardoen, Void growth and coalescence in ductile solids with stage III and stage IV strain hardening, *International Journal of Plasticity* 27 (2011) 1203–1223. doi:10.1016/j.ijplas.2011.01.004.
- [45] R. A. Lebensohn, Y. Liu, P. P. Castañeda, On the accuracy of the self-consistent approximation for polycrystals: Comparison with full-field numerical simulations, *Acta Materialia* 52 (2004) 5347–5361. doi:10.1016/j.actamat.2004.07.040.
- [46] T. Francis, P. F. Rottmann, A. T. Polonsky, M.-A. Charpagne, M. P. Echlin, V. Livescu, D. Jones, G. Gray, M. De Graef, T. M. Pollock, Multimodal 3D characterization of voids in shock-loaded tantalum: Implications for ductile spallation mechanisms, *Acta Materialia* 215 (2021) 117057. doi:10.1016/J.ACTAMAT.2021.117057.
- [47] E. J. Lieberman, R. A. Lebensohn, D. B. Menasche, C. A. Bronkhorst, A. D. Rollett, Microstructural effects on damage evolution in shocked copper polycrystals, *Acta Materialia* 116 (2016) 270–280. doi:10.1016/J.ACTAMAT.2016.06.054.
- [48] R. Pokharel, R. A. Lebensohn, D. C. Pagan, T. L. Ickes, B. Clausen, D. W. Brown, C.-F. Chen, D. S. Dale, J. V.

Bernier, In-Situ Grain Resolved Stress Characterization During Damage Initiation in Cu-10%W Alloy, JOM 2019 72:1 72 (2019) 48–56. URL: <https://link.springer.com/article/10.1007/s11837-019-03692-5>. doi:10.1007/S11837-019-03692-5.

- [49] D. P. Naragani, J. S. Park, P. Kenesei, M. D. Sangid, Void coalescence and ductile failure in IN718 investigated via high-energy synchrotron X-ray tomography and diffraction, Journal of the Mechanics and Physics of Solids 145 (2020). doi:10.1016/J.JMPS.2020.104155.